Article:

Pei, Y., Su, Q., Liu, K. et al. (5 more authors) (2025) Modelling the dynamics of ballastless railway tracks on unsaturated subgrade. Applied Mathematical Modelling, 138 (Part B). 115801. ISSN 0307-904X

https://doi.org/10.1016/j.apm.2024.115801

Modelling the dynamics of ballastless railway tracks on unsaturated subgrade

Yanfei Pei[a], Qian Su[a,b], Kaiwen Liu[a,b*], David P. Connolly[c], Bao Liu[d], Rui Su[e], Zongyu Zhang[a], Tengfei Wang[a]

[a] School of Civil Engineering, Southwest Jiaotong University, Chengdu, Sichuan 610031, China

[b] Key Laboratory of High-Speed Railway Engineering of Ministry of Education, Southwest Jiaotong University, Chengdu, Sichuan 610031, China

[c] Institute for High Speed Rail and Systems Integration, School of Civil Engineering, University of Leeds, UK.

[d] China Railway Design Corporation, Tianjin, 300308, China

[e] School of Architecture and Civil Engineering, Xihua University, Chengdu, Sichuan 610039, China

*Corresponding author, email: kaiwen.liu@queensu.ca

Abstract:

Concrete slab tracks help shield the supporting railway trackbed from external water ingress. However, the inevitable cracks that arise during its lifespan provide a pathway for water penetration, leading to changes in the degree of saturation of the underlying support. This can affect the dynamic response of the structure, however is challenging to model due to the computational requirements of three-phase unsaturated soil simulation. To address this, this paper presents two main novelties: 1) an efficient moving frame of reference approach for railway ballastless tracks on unsaturated earthworks subject to train loading, 2) new findings into the effect of degree of trackbed saturation on ballastless track dynamics. First the model is presented, including formulations for train-track interaction and unsaturated trackbed-earthwork dynamics. Considerations for numerical stability are then discussed and the model is validated, before investigating the role of trackbed saturation on pore water pressure and displacements. It is shown to have a high impact on pore water pressure generation, but a limited impact on deflections. The effect of train speed is then investigated and it is found that higher train speeds induce higher pore water pressures. Track irregularities are also investigated and it is found that they play an important role in pore water pressures.

Keywords: High-speed railway, Ballastless railway track, Unsaturated rail trackbed, Moving mixed element method, Train-track dynamic response, Railway moisture content

1 Introduction

The popularity of ballastless tracks, particularly for high-speed railways, has increased in recent years due to perceived advantages compared to ballasted track, such as reduced maintenance. Notably, the majority of high-speed railway track designs in Germany, Japan, and China exclusively use ballastless track [1, 2]. However, ballastless track is typically formed from concrete, which in the long-term, experiences cracking due to repeated train and thermal loading. This has been found on the Japan Tokaido Shinkansen [3] and in Germany [4]. Once cracked, rainwater can infiltrate the trackbed that is a key structural layer of ballastless railway subgrade (Fig. 1), leading to changes in the degree of saturation within the trackbed and underlying earthworks [5]. With rainwater trapped or groundwater rising into the trackbed, it undergoes wetting and drying cycles which cause challenges including: mud pumping, frost heave, and differential settlement [6] [7-9]. Many trackbed engineering defects are closely related to the degree of saturation internally. The pore water pressure resulting from train loading produces internal erosion and transports the fine particles inside the trackbed, which in the long-term exacerbates mud pumping and differential settlement [10]. Therefore, it is important to better understand the hydrodynamic responses induced within trackbeds under varying water content.

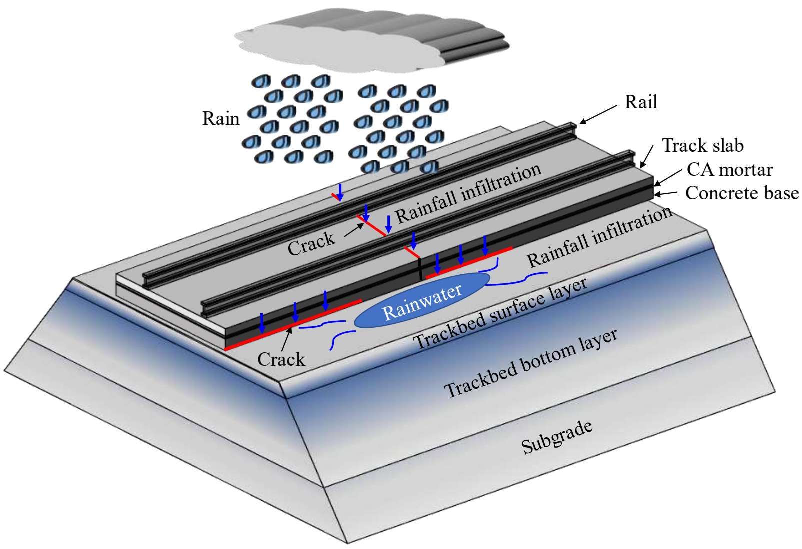

Fig. 1 Infiltration of rainwater and evolution of water content within a ballastless trackbed

The effect of water on the dynamic response of soils was first studied considering a fully saturated state. Biot [11, 12] first proposed the theory of elastic wave motion in saturated porous media, which later became widely used to study saturated soils [13, 14]. The number of solution variables in saturated porous media are more than twice as many compared to single-phase (i.e. dry) media. Four computational approaches have been proposed to study the response of saturated porous media under dynamic loading: ① $u-U$, ② $u-w$, ③ $u-U-p$, and ④ $u-p$ [15, 16], where the variables u, U, w, and p represent the displacement of the solid, absolute displacement of the fluid, relative displacement of the fluid, and pore fluid pressure, respectively. According to the physical properties of the variables in the governing equations, the four coupling formats are classified as mixed (③④) and displacement formats (①②). According to considering or not the relative acceleration term of the pore fluid, they are classified into full (①②③) and partially coupled formats (④) [17]. Their main differences are as follows: (1) seepage boundary. The $u-U$ and $u-w$ formats cannot be directly defined based on pore fluid pressure when establishing the free seepage boundary (i.e. p=0). In contrast, the $u-U-p$ and $u-p$ formats possess distinct physical significance and can be easily implemented through the use of the Dirac boundary; (2) frequency of external loads. The $u-p$ model simplifies the momentum conservation equation by assuming the relative acceleration term of the fluid generates zero inertia force ($\ddot{w}=0$) [18]. However, this kind of simplification will bring large error under the action of high frequency load. Errors are acceptable under low frequency loads. (3) numerical stability. When using $u-U$ or $u-w$ format, the lower-order element may have numerical problems such as shear locking. In contrast, this numerical oscillation removal technique is perhaps more complex. In a comparison, using a mixed format such as $u-U-p$ or $u-p$ can solve easily such problems. These models have been used to analyse the dynamic response of saturated road foundations and roadbeds [19-22]. Currently, dynamic calculation methods for unsaturated trackbeds primarily focus on using analytical/semi-analytical solutions [23-25] and traditional FEM [26].

Analytical and semi-analytical solutions are typically computed in the frequency-wavenumber domain which makes it challenging to consider wheel-rail non-linear contact and non-linear soil stiffness or damping. Further, irregular geometries and complex seepage boundary conditions can be difficult to simulate depending upon the approach. To overcome some of the irregular geometry challenges, the 2.5D FEM has also been proposed [27-29] however this assumes material parameters do not vary in the train passage direction. In order to express the complex characteristics of the coupled vehicle-track system and at the same time to maximise computational efficiency, this paper proposed the moving element method. This uses a moving frame transformation, which allows the train or other moving loads to be relatively stationary and the substructure to be in a "flow" state. The method, which has been gradually developed in recent years, has been used to study the dynamic response of coupled train-track systems and plate-shell dynamics [30-33]. However, it has only been used for single-phase mediums and not for unsaturated porous medium analysis. In conclusion, there remains a gap in the computational methods available for the fast and flexible analysis of coupled vehicle-track-unsaturated trackbed systems.

Considering these aforementioned approaches, this study proposes a fast method for solving the dynamic response of a coupled vehicle-track-unsaturated trackbed system, which can consider a wider range of geometries and non-linearity's. To do so the dynamic equations of motion are established using the D'Alembert principle and nonlinear Hertz contact is employed to describe the wheel-rail interaction. A mixed element method is established using a geometric transformation method. The governing equations and boundary conditions of the unsaturated trackbed are derived in a fully coupled format, considering the dynamic nature of the system and a moving coordinate system, while the Ladyshenskaya-Babuska-Brezzi (LBB) technique is used to overcome the numerical oscillation of the mixed element. The accuracy and efficiency of the calculation method are verified. Lastly the dynamic response of unsaturated trackbeds is further analyzed, considering the effects of wavelength and track irregularity amplitude, degree of saturation, and train speed.

2 Numerical model development

This section is related to the development of a train-track-subgrade model in a moving frame of reference. First an overview is given describing the mixed frame of reference concept which is vital for reducing the computational demand of the three-phase unsaturated soil model. Next the equations related to the train, track and their coupling are presented. Finally, the modelling approach used to simulate the unsaturated earthworks supporting the track is presented.

2.1 Model overview

In order to establish a mathematical model, this section introduces the interrelationships between the vehicle subsystem, the track subsystem, and the unsaturated trackbed subsystem (**Error! Reference source not found.**Fig. 2). Initially, the dynamic governing equations for the vehicle are formulated, followed by the coupling with the ballastless track, considering non-linear Hertz contact between the wheel and rail. Coupling with the unsaturated trackbed is achieved via a coupled multi-physics mathematical model, incorporating mass conservation, momentum conservation and constitutive relationships. Finally, a coupled mathematical model of the vehicle-track-trackbed system is constructed based on the moving mixed element approach. Additionally, a rapid computational method is used to analyze the hydraulic response of the unsaturated trackbed under the influence of train loading.

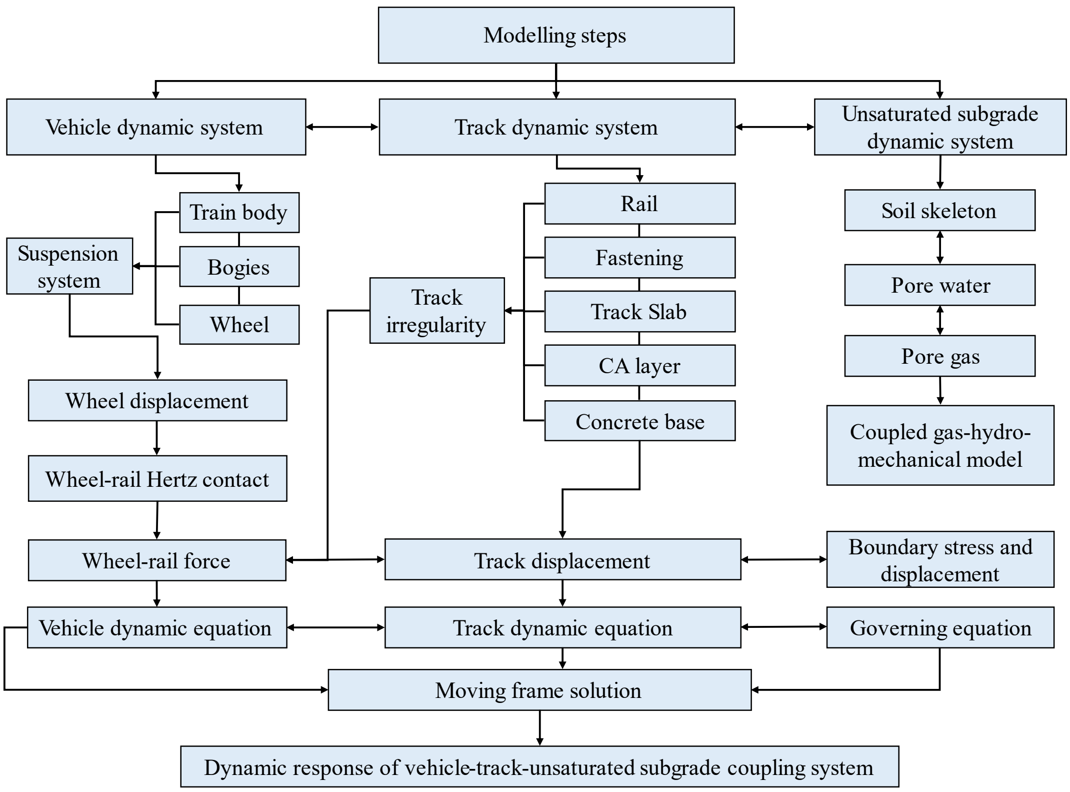

Fig. 2 Flowchart of the vehicle-track-unsaturated trackbed model

2.2 Moving frame of reference

In order to add seepage boundaries on a freely permeable surface and to overcome the complexities of numerical stabilisation, a u-U-p format is used for mathematical modelling of the unsaturated trackbed. Meanwhile, in order to improve the solution efficiency of the vehicle-track-unsaturated trackbed model, the system is calculated based on a moving coordinate system.

The high-speed train moves in the x direction, with point O serving as the fixed position. $F(t)$ represents the interaction force between the train's wheels and the rails. Assuming the train speed is v, a moving coordinate system denoted as $R = x - v \cdot t$ is fixed on the train. Fig. 3 illustrates the model overview.

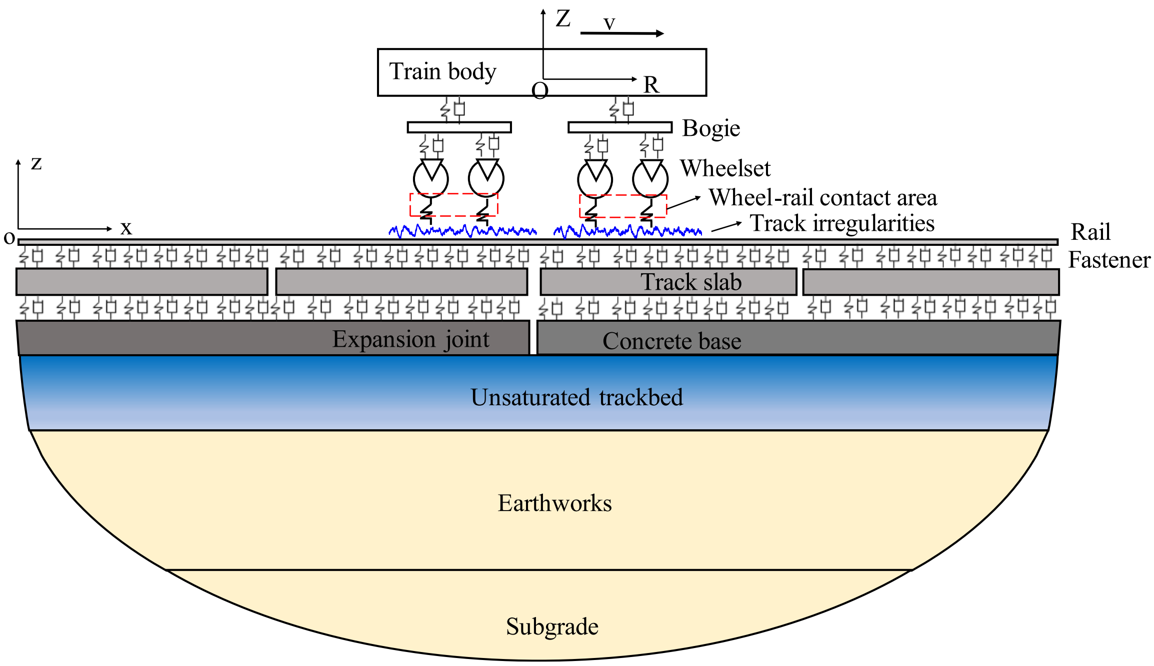

Fig. 3 Mathematical modeling of the vehicle-track-unsaturated subgrade coupling system in a moving frame

In the fixed coordinate system $oxyz$ and the moving coordinate system $ORYZ$ used for the train, the field variables are interrelated:

$$\begin{cases} \dfrac{\partial}{\partial x} = \dfrac{\partial}{\partial R} \\ \dfrac{\partial}{\partial x^2} = \dfrac{\partial}{\partial R^2} \\ \left.\dfrac{\partial}{\partial t}\right|_x = \left.\dfrac{\partial}{\partial t}\right|_R - v\dfrac{\partial}{\partial R} \\ \left.\dfrac{\partial}{\partial t^2}\right|_x = \left.\dfrac{\partial}{\partial t^2}\right|_R - 2v\dfrac{\partial}{\partial t \partial R} + v^2\dfrac{\partial}{\partial R^2} \end{cases} \tag{1}$$

2.3 Ballastless track subsystem

A Euler-Bernoulli beam is employed to simulate each rail [34]. Applying the aforementioned variable transformation method, the governing equations of this beam under the moving coordinate system are:

$$E_r I_r \frac{\partial^4 y_r}{\partial R^4} + m_r\left(\frac{\partial^2 y_r}{\partial t^2} + v^2\frac{\partial^2 y_r}{\partial R^2} - 2v\frac{\partial^2 y_r}{\partial R \partial t}\right) + c_r\left(\frac{\partial y_r}{\partial t} - v\frac{\partial y_r}{\partial R} - \left(\frac{\partial y_s}{\partial t} - v\frac{\partial y_s}{\partial R}\right)\right) + k_r(y_r - y_s) = -F(t)\delta(R) \quad (2)$$

Where y_r and y_s are the vertical displacement of the rail and track slab, respectively; $E_r I_r$ is the bending stiffness of the rail; m_r is the mass of the rail per unit length; k_r and c_r are the coefficients of the fastener stiffness and damping; F(t) is the wheel-rail contact force; v is the train speed; δ is the Dirac function. The Navier-elastic dynamic equation is employed to describe the motion of the ballastless track slab and concrete base:

$$\frac{\partial \sigma_{ij}}{\partial x_i} = \rho_i \frac{\partial^2 u_i}{\partial t^2} - 2\rho_i v \frac{\partial^2 u_i}{\partial R \partial t} + \rho_i v^2 \frac{\partial^2 u_i}{\partial R^2} \quad (3)$$

Where σ is the stress tensor in the track slab and concrete base, ρ is the density of the track slab and concrete base, and u is the displacement of the track slab and concrete base.

2.4 Vehicle subsystem

2.4.1 Vehicle dynamic equation

The high-speed vehicle dynamics model includes the vehicle body, two bogies, and four wheelsets. Using multi-body dynamics theory, the model has 10 degrees of freedom, as depicted in Fig. 4. The degrees of freedom are the vertical displacement (v) and the pitch angle (θ). Applying D'Alembert's principle, the dynamic governing equations can be established.

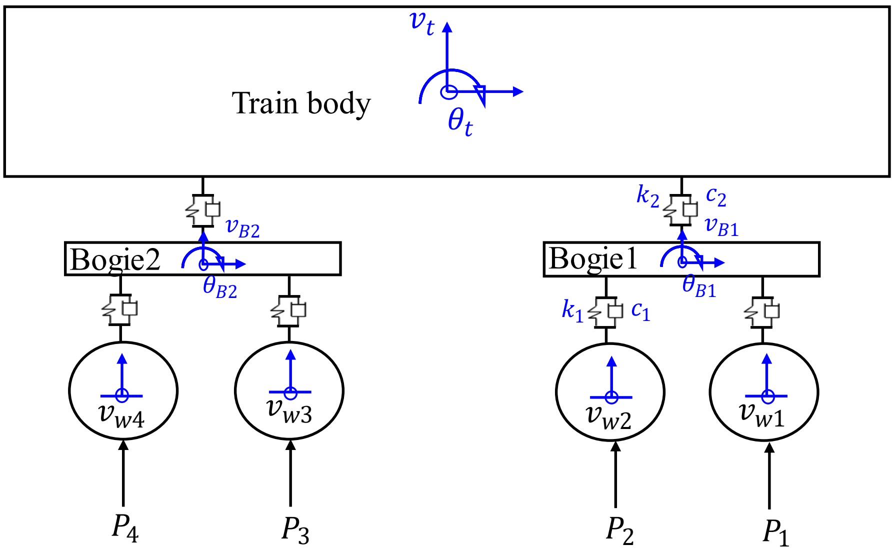

Fig. 4 Multibody vehicle model

(1) Vibration of the vehicle body:

The vertical vibration is derived from the force equilibrium of the vehicle:

$$M_t \ddot{v}_t + C_2\left[\left(\dot{v}_t - \dot{v}_{B1} - \dot{\theta}_t l_t\right) + \left(\dot{v}_t - \dot{v}_{B2} + \dot{\theta}_t l_t\right)\right] + K_2\left[\left(v_t - v_{B1} - \theta_t l_t\right) + \left(v_t - v_{B1} + \theta_t l_t\right)\right] + M_t g = 0 \quad (4)$$

The pitch motion is as follows:

$$J_t \ddot{\theta}_t + C_2 l_t\left[-\left(\dot{v}_t - \dot{v}_{B1} - \dot{\theta}_t l_t\right) + \left(\dot{v}_t - \dot{v}_{B2} + \dot{\theta}_t l_t\right)\right] + K_2 l_t\left[-\left(v_t - v_{B1} - \theta_t l_t\right) + \left(v_t - v_{B1} + \theta_t l_t\right)\right] = 0 \quad (5)$$

(2) Vibration of the bogie:

The vertical vibration is based on the force balance of the bogie:

$$M_B\ddot{v}_{Bi}-C_2(\dot{v}_t-\dot{v}_{Bi}-\dot{\theta}_t l_t)+C_1\left[(v_{Bi}-v_{wj}-\theta_{Bi}l_b)+(v_{Bi}-v_{wj+1}+\theta_{Bi}l_b)\right]-K_2(v_t-v_{Bi}-\dot{\theta}_t l_t)$$
$$+K_1\left[(v_{Bi}-v_{wj}-\theta_{Bi}l_b)+(v_{Bi}-v_{wj+1}+\theta_{Bi}l_b)\right]+M_t g=0 \tag{6}$$

Again, the equations of pitch motion are then:

$$J_t\ddot{\theta}_{B1}+C_1 l_b\left[-(\dot{v}_{B1}-\dot{v}_{w1}-\dot{\theta}_{B1}l_b)+(\dot{v}_{B1}-\dot{v}_{w2}+\dot{\theta}_{B1}l_b)\right]$$
$$+K_1 l_b\left[-(v_{B1}-v_{w1}-\theta_{B1}l_b)+(v_{B1}-v_{w2}+\theta_{B1}l_b)\right]=0 \tag{7}$$

$$J_t\ddot{\theta}_{B2}+C_1 l_b\left[-(\dot{v}_{B2}-\dot{v}_{w3}-\dot{\theta}_{B2}l_b)+(\dot{v}_{B2}-\dot{v}_{w4}+\dot{\theta}_{B2}l_b)\right]$$

$$+K_1 l_b\left[-(v_{B2}-v_{w3}-\theta_{B2}l_b)+(v_{B2}-v_{w4}+\theta_{B2}l_b)\right]=0 \tag{8}$$

(3) Vibration of the wheelset:

The vertical vibration is based on the force equilibrium of the wheelset:

$$\begin{cases} M_{wi}\ddot{v}_{wi}-C_1(\dot{v}_{Bi}-\dot{v}_{wi}-\dot{\theta}_{Bi}l_t)-K_1(v_{Bi}-v_{wi}-\theta_{Bi}l_t)=P_i \quad (i=1,3) \\ M_{wj}\ddot{v}_{wj}-C_1(\dot{v}_{Bi}-\dot{v}_{wj}+\dot{\theta}_{Bi}l_t)-K_1(v_{Bi}-v_{wj}+\theta_{Bi}l_t)=P_j \quad (j=2,4) \end{cases} \tag{9}$$

Where M_t is the mass of the train body; C_1 is the damping of the primary suspension and K_1 is the stiffness of the primary suspension; C_2 is the damping of the secondary suspension and K_2 is the stiffness of the secondary suspension. When the ordering of the wheelset is an odd number ($i=1,2,3,4; j=1,2$), the plus or minus sign ($\pm$) is minus (-).

The equations relating to vehicle dynamics can be presented in matrix form:

$$\boldsymbol{M_V}\ddot{\boldsymbol{u}}_{\boldsymbol{V}}+\boldsymbol{C_V}\dot{\boldsymbol{u}}_{\boldsymbol{V}}+\boldsymbol{K_V}\boldsymbol{u_V}=\boldsymbol{Q_V} \tag{10}$$

Where $\boldsymbol{M_V}$, $\boldsymbol{C_V}$, $\boldsymbol{K_V}$ are the mass, damping and stiffness matrices of the vehicle expanded above and $\boldsymbol{u_V}$ is the degree of freedom of the vehicle system. $\boldsymbol{Q_V}$ is the load matrix consisting of the gravity and wheel-rail force. The specific matrix expansion form can be found in [35, 36].

2.4.2 **Wheel-rail contact relationship**

The contact force between the wheels and rails can be calculated by employing non-linear Hertz contact theory:

$$F_{wri}(t)=\begin{cases} \dfrac{1}{G^{\frac{3}{2}}}\left|z_{wi}-(z_{ri}+\Delta z)\right|^{\frac{3}{2}}, & z_{wi}-(z_{ri}+\Delta z)<0 \\ 0, & z_{wi}-(z_{ri}+\Delta z)\geq 0 \end{cases} \tag{11}$$

Where $P_i=-M_w g+F_{wri}$. F_{wri} is the dynamic wheel-rail contact force, z_{wi} is the displacement of a train wheel moving on the rail at position x_i, z_{ri} is the displacement of the wheel moving on the rail at position x_i, Δz is the value of the track irregularity, and G is the deflection coefficient of the wheel-rail contact ($G=4.57R^{-0.149}\times 10^{-8}\left(m/N^{\frac{2}{3}}\right)$). The external profile of the wheel is assumed a conical surface.

2.5 Unsaturated trackbed and earthworks subsystem

After ballastless track cracking, rainwater infiltrates the layers below. Hence, the scenario where the surface layer of the trackbed is in an unsaturated state is considered. To describe the dynamic behavior of an unsaturated trackbed, the governing equation takes the form of full-coupling: $u-U-p$. This form is chosen to avoid errors at high frequency train loading and the challenges associated with adding free seepage boundaries such as shear locking. The governing equations for the multiphysical field coupling of an unsaturated trackbed are presented below.

2.5.1 **Constitutive equation**

The trackbed consists of three components: soil, water and gas. As a result, the total stress in the unsaturated medium can be represented via:

$$\sigma_{ij} = (1-n)\sigma_{ij}^{s} - nS_r p^w \delta_{ij} - n(1-S_r)p^a \delta_{ij} \tag{12}$$

According to the effective stress principle proposed by Biot and Bishop [37], the total stress within an unsaturated trackbed can be represented as:

$$\sigma_{ij} = 2\mu\epsilon_{ij} + \lambda\delta_{ij}e - \alpha\delta_{ij}p \tag{13}$$

Where n is the porosity of the trackbed, S_r represents the degree of saturation, $p = S_r p^w + (1-S_r)p^a$ is the pore fluid pressure, p^w is the pore water pressure, p^a is the pore gas pressure, $\alpha = 1 - \frac{K_b}{K_s}$ is Biot's coefficient where K_b and K_s are the bulk compression modulus of the soil skeleton and the soil particles, μ and λ are Lame parameters, e is the volumetric strain, and ϵ_{ij} is the strain tensor of the soil skeleton.

Using constitutive equations (12) and (13), the solid phase pressure can be obtained:

$$\sigma_{ij}^{s} = \frac{1}{(1-n)}\left\{\lambda\delta_{ij}e + 2\mu\epsilon_{ij} - [\alpha S_r - nS_r]\delta_{ij}p^w - [\alpha(1-S_r) - n(1-S_r)]\delta_{ij}p^a\right\} \tag{14}$$

2.5.2 **Mass conservation equation**

(1) Mass conservation equation for the trackbed

The mass conservation equation for the trackbed is established based on the principle of mass conservation in porous media.

$$(1-n)\frac{\partial\rho_s}{\partial t} - \rho_s\frac{\partial n}{\partial t} + \rho_s(1-n)\nabla\cdot\dot{\boldsymbol{u}}^s = 0 \tag{15}$$

Concurrently, the analysis incorporates the compressible nature of the solid material, and as a result, the compressive state equations are [38]:

$$\frac{\partial\rho_s}{\rho_s\partial t} = -\frac{\partial\sigma_{ii}^{s}}{3K_s\partial t} \tag{16}$$

Subsequently, using equations (14), (15), and (16), the governing equations capturing the temporal variation of the trackbed porosity are derived as:

$$\frac{\partial n}{\partial t} = \left(1 - n - \frac{K_b}{K_S}\right)\nabla\cdot\dot{\boldsymbol{u}}^s + \frac{(\alpha S_r - n\,S_r)}{K_S}\frac{dp^w}{dt} + \frac{\big(\alpha(1-S_r) - n(1-S_r)\big)}{K_S}\frac{dp^a}{dt} \tag{17}$$

(2) Mass conservation equation for water in the trackbed

According to the principle of mass conservation in continuous media, the equation for the mass conservation of pore-water in the trackbed is established:

$$nS_r\frac{\partial\rho_w}{\partial t} + S_r\rho_w\frac{\partial n}{\partial t} + n\rho_w\frac{\partial S_r}{\partial t} + nS_r\rho_w\nabla\cdot\dot{\boldsymbol{u}}^w = 0 \tag{18}$$

Equation (17), which includes the compression state equation for water $\frac{\partial \rho_w}{\rho_w \partial t} = \frac{\partial p^w}{K_w \partial t}$ [38], is incorporated into (18) to derive the equation for mass conservation of pore-water in the moving coordinate system.

$$\alpha S_r \nabla\left(\dot{u}_i^s - v u_{i,R}^s\right) + n S_r \nabla\left[\left(\dot{u}_i^w - v u_{i,R}^w\right) - \left(\dot{u}_i^s - v u_{i,R}^s\right)\right] + a_1\left(\dot{p}^w - v p_{,R}^w\right) + a_2\left(\dot{p}^a - v p_{,R}^a\right) = 0 \tag{19}$$

(3) Mass conservation equation for gas in the trackbed

Based on the principle of mass conservation in continuous media, the equation for the mass conservation of pore-gas in the trackbed is:

$$n(1 - \mathrm{S_r})\frac{\partial \rho_a}{\rho_a \partial t} + (1 - \mathrm{S_r})\frac{\partial n}{\partial t} + n\frac{\partial (1 - S_r)}{\partial t} + n(1 - \mathrm{S_r})\nabla \cdot \dot{\boldsymbol{u}}^{\boldsymbol{a}} = 0 \tag{20}$$

Incorporating Equation (17) into (20), which includes the compression state equation for gas $\frac{\partial \rho_a}{\rho_a \partial t} = \frac{\partial p^a}{K_a \partial t}$ [38], the equation for conserving the mass of pore-gas in the moving coordinate system is derived as:

$$\alpha(1 - S_r)\nabla\left(\dot{u}_i^s - v u_{i,R}^s\right) + n(1 - S_r)\nabla\left[\left(\dot{u}_i^a - v u_{i,R}^a\right) - \left(\dot{u}_i^s - v u_{i,R}^s\right)\right] + b_1\left(\dot{p}^w - v p_{,R}^w\right) + b_2\left(\dot{p}^a - v p_{,R}^a\right) = 0 \tag{21}$$

The van Genuchten model is employed [39] to derive the relationship between matrix suction and the degree of saturation in unsaturated porous media:

$$S_e = [1 + (\alpha_2 s)^d]^{-m} \tag{22}$$

$$S_e = (S_r - S_{w0})/(1 - S_{w0}) \tag{23}$$

Where S_e is the effective saturation of the trackbed and S_{w0} is the residual saturation of the trackbed.

2.5.3 **Momentum conservation equation**

(1) Momentum conservation equation for trackbed

The momentum of the representative volume element (RVE) changes at a rate equal to the sum of the external forces acting on it. Therefore, the equation for the moving mixed form of the trackbed is:

$$\sigma_{ij,j} = \sum \bar{\rho}_\Theta \left(\ddot{u}_i^\Theta - 2v\dot{u}_{i,R}^\Theta + v^2 u_{i,RR}^\Theta\right) \tag{24}$$

Where Θ represents the soil skeleton, pore water, and pore gas, respectively, and $\bar{\rho}_m$ is the average density of the soil skeleton, pore water, and pore gas, respectively.

(2) Momentum conservation equation for pore water

The rate of change of momentum for the pore water in a RVE is equal to the sum of the external forces acting on it. Therefore, the equation for the moving mixed form of the pore water is:

$$-p_{,i}^w = \rho_w\left(\ddot{u}_i^w - 2v\dot{u}_{i,R}^w + v^2 u_{i,RR}^w\right) + \frac{n S_r \mu_w}{k_{rw} k}\left(\dot{u}_i^w - v u_{i,R}^w\right) - \frac{n S_r \mu_w}{k_{rw} k}\left(\dot{u}_i^s - v u_{i,R}^s\right) \tag{25}$$

Where k_{rw} is the relative permeability coefficient of the pore water, μ_w is the dynamic viscosity coefficient of the pore water and k is the intrinsic permeability of the porous medium.

(3) Momentum conservation equation for pore gas

The rate of change of the momentum of pore gas in a RVE is equal to the sum of the external forces acting on the porous gas of the RVE. Thus, the moving mixed form of the pore gas is:

$$-p_{,i}^{a} = \rho_a\left(\ddot{u}_i^a - 2v\dot{u}_{i,R}^a + v^2 u_{i,RR}^a\right) + \frac{n(1-S_r)\mu_a}{k_{ra}k}\left(\dot{u}_i^a - vu_{i,R}^a\right) - \frac{n(1-S_r)\mu_a}{k_{ra}k}\left(\dot{u}_i^s - vu_{i,R}^s\right) \tag{26}$$

Where k_{ra} is the relative permeability coefficient of the pore gas, μ_a is the dynamic viscosity coefficient of the pore gas, and k is the intrinsic permeability of the porous medium.

The calculation parameters of ballastless trackbed are shown in Table 1.

Table 1 Calculation parameters for unsaturated trackbed

Parameters	Structural layer		
	Trackbed surface layer	Lower layer	Subgrade body
Thickness (m)	0.4	2.3	1.2
Elastic modules E(MPa)	250	180	150
Poisson's ratio ν	0.25	0.3	0.35
Solid densityρ_s(kg/m^3)	2300	2000	1950
Water density ρ_w(kg/m^3)	1000	-	–
Gas density ρ_a(kg/m^3)	1.29	-	
Soil porosity n	0.25	–	–
Compressibility factor α	0.95	–	–
Water viscosity μ_w ($Pa\cdot s$)	0.001	–	–
Gas viscosity μ_a ($Pa\cdot s$)	1.5075×10^{-5}	-	-
Permeability k(m^2)	10^{-11}	–	–
Effective stress parameter(φ)	Sr	-	-
Bulk modulus(K_w)(GPa)	2.20	-	-
Bulk modulus(K_a)(kPa)	145	-	-
The fitting parameters of unsaturated trackbed (α_2)	8.08		
The fitting parameter of unsaturated trackbed (d)	1.66		
The fitting parameters of unsaturated trackbed (m)	1-1/d		

3 Model solver

After formulating the interconnected model of the vehicle, track, and unsaturated trackbed system, the governing equations are discretized. In order to perform non-linear computations, the Newton-Raphson method is applied, with time integration handled using a second-order backward difference method. The implicit integration method is described in detail in [40, 41].

3.1 Vehicle-track system

Multiplying the governing equation of the Euler-Bernoulli beam by a test function $\delta \boldsymbol{y_r}$ yields the following form:

$$\int_0^L \delta \boldsymbol{y_r} \cdot \left(E_r I_r \frac{\partial^4 y_r}{\partial R^4} + m_r \left(\frac{\partial^2 y_r}{\partial t^2} + v^2 \frac{\partial^2 y_r}{\partial R^2} - 2v \frac{\partial^2 y_r}{\partial R \partial t} \right) + c_r \left(\frac{\partial y_r}{\partial t} - v \frac{\partial y_r}{\partial R} - \left(\frac{\partial y_s}{\partial t} - v \frac{\partial y_s}{\partial R} \right) \right) + k_r (y_r - y_s) + F(t)\delta(R) \right) dR = 0$$

The mass, damping and stiffness matrices of the rail can be obtained through the use of the Gauss-Green formula after discretization:

$$\boldsymbol{M_r^e} = m_r \int_0^L \boldsymbol{N_r^T N_r} \mathrm{dR}$$

$$\boldsymbol{C_r^e} = -2m_r v \int_0^L \boldsymbol{N_r^T N_{r,R}} \mathrm{dR} + c_r \int_0^L \boldsymbol{N_r^T N_r} \mathrm{dR} - c_r \int_0^L \boldsymbol{N_r^T N_{su}} \mathrm{dR}$$

$$\boldsymbol{K_r^e} = E_r I_r \int_0^L \boldsymbol{N_{r,RR}^T N_{r,RR}} \mathrm{dR} - m_r v^2 \int_0^L \boldsymbol{N_{r,R}^T N_{r,R}} \mathrm{dR} - c_r v \int_0^L \boldsymbol{N_r^T N_{r,R}} \mathrm{dR} + c_r v \int_0^L \boldsymbol{N_r^T N_{su,R}} \mathrm{dR} + k_r \int_0^L \boldsymbol{N_r^T N_r} \mathrm{dR} - k_r \int_0^L \boldsymbol{N_r^T N_{su}} \mathrm{dR}$$

Where $\boldsymbol{N_r}$ is the shape function of the rail and $\boldsymbol{N_{su}}$ is the shape function of the track slab.

In the context of a ballastless track system, the governing equations of the track slab and the concrete base can be multiplied by the test function $\delta \boldsymbol{u}$ and transformed into an equivalent weak-form integral. This transformation leads to:

$$-\int_\Omega \delta \boldsymbol{u}\, \sigma_{ij,j} d\Omega + \rho_i \int_\Omega \delta \boldsymbol{u}\, \ddot{u}_i d\Omega - 2v\rho_i \int_\Omega \delta \boldsymbol{u}\, \ddot{u}_{i,R} d\Omega + v^2 \rho_i \int_\Omega \delta \boldsymbol{u}\, \ddot{u}_{i,RR} d\Omega = 0$$

The above equation is integrated using the Gauss-Green formula to obtain:

$$\int_\Omega \delta \boldsymbol{u}_{,i}\, \sigma_{ij} d\Omega + \rho_i \int_\Omega \delta \boldsymbol{u}\, \ddot{u}_i d\Omega - 2v\rho_i \int_\Omega \delta \boldsymbol{u}\, \ddot{u}_{i,R} d\Omega + v^2 \rho_i \int_\Omega \delta \boldsymbol{u}\, \ddot{u}_{i,RR} d\Omega = \int_\Gamma n_i \sigma_{ij} \delta \boldsymbol{u}\, d\Gamma$$

This results in the form of a flow element for the track slab and the concrete base:

$$\boldsymbol{M_i^e \ddot{u}_i} + \boldsymbol{C_i^e \dot{u}_i} + \boldsymbol{K_i^e u_i} = \boldsymbol{f_i^e} \tag{27}$$

The mass, damping, and stiffness matrices of the track slab and concrete base can be obtained by discretizing them as:

$$\boldsymbol{M_i^e} = \rho_i \int_\Omega \boldsymbol{N_{iu}^T N_{iu}}\, d\Omega;$$

$$\boldsymbol{C_i^e} = -2\rho_i v \int_\Omega \boldsymbol{N_{iu}^T N_{iu,R}}\, d\Omega;$$

$$\boldsymbol{K_i^e} = \int_\Omega \boldsymbol{B_{iu}^T D_{iu} B_{iu}} d\Omega + \rho_i v^2 \int_\Omega \boldsymbol{N_{iu}^T N_{iu,RR}}\, d\Omega;$$

$$\boldsymbol{f_i^e} = \int_\Gamma \boldsymbol{N_{iu}^T \sigma^e} d\Omega;$$

Where the subscript $i = (s, c)$ represents the track slab and concrete base, $\boldsymbol{M_i^e}$, $\boldsymbol{K_i^e}$, $\boldsymbol{C_i^e}$ are the mass, stiffness and damping matrices of the track slab and concrete base, respectively, $\boldsymbol{N_{iu}}$ is the shape function of the track slab and the concrete base, $\boldsymbol{B_{iu}}$ is the strain matrix of the track slab and the concrete base, $\boldsymbol{D_{iu}}$ is the elasticity matrix of the track slab and the concrete base, and $\boldsymbol{\sigma^e}$ is the boundary stress of the track slab and the concrete base.

3.2 The unsaturated trackbed

The Galerkin weighted residual method is used to obtain the equivalent weak form integral of the multi-field coupled equations for the unsaturated trackbed. In this method, various shape functions are employed to represent the different displacement and pressure fields. The shape functions are as follows: $u^s = \boldsymbol{N_u u}$ is the representation of the shape function for the displacement of the trackbed soil, $u^w = \boldsymbol{N_w U_w}$ is the representation of the shape function for the displacement of the pore water, $u^a = \boldsymbol{N_a U_a}$ is the representation of the shape function for the displacement of the pore gas, $p^w = \boldsymbol{N_p^w p^w}$ is the representation of the shape function for the pore water pressure, and $p^a = \boldsymbol{N_p^a p^a}$ is the representation of the shape function for the pore gas pressure. These shape functions, denoted by $\boldsymbol{N_u}, \boldsymbol{N_w}, \boldsymbol{N_a}, \boldsymbol{N_p^w}\ \boldsymbol{and N_p^a}$, describe the absolute displacement of the soil, the absolute displacement of the pore water, the absolute displacement of the pore gas, the pore water pressure, and the pore gas pressure respectively.

Using the discrete version of the displacement of the trackbed soil, $u = \boldsymbol{N_u u}$, the discrete version of the pore water pressure, $p^w = \boldsymbol{N_p^w p^w}$, and the discrete version of the pore gas pressure, $p^a = \boldsymbol{N_p^a p^a}$, the overall equation of motion for the trackbed structure can be expressed in a discrete format (see Appendix A for derivation):

$$\boldsymbol{M_s \ddot{u}} + \boldsymbol{M_{sw} \ddot{U}_w} + \boldsymbol{M_{sa} \ddot{U}_a} + \boldsymbol{C_s \dot{u}} + \boldsymbol{C_{sw} \dot{U}_w} + \boldsymbol{C_{sa} \dot{U}_a} + \boldsymbol{K_s u} + \boldsymbol{K_{sw} U_w} + \boldsymbol{K_{sa} U_a} - \boldsymbol{Q p^w} - \boldsymbol{R p^a} = \boldsymbol{f^u} \tag{28}$$

Where the mass, damping and stiffness matrices are:

$\boldsymbol{M_s} = \bar{\rho}_s \int_\Omega \boldsymbol{N_u^T N_u} d\Omega$, $\boldsymbol{M_{sw}} = \bar{\rho}_w \int_\Omega \boldsymbol{N_u^T N_w} d\Omega$, $\boldsymbol{M_{sa}} = \bar{\rho}_a \int_\Omega \boldsymbol{N_u^T N_a} d\Omega$

$\boldsymbol{C_s} = -2v\bar{\rho}_s \int_\Omega \boldsymbol{N_u^T N_{u,R}} d\Omega$, $\boldsymbol{C_{sw}} = -2v\bar{\rho}_w \int_\Omega \boldsymbol{N_u^T N_{w,R}} d\Omega$, $\boldsymbol{C_{sa}} = -2v\bar{\rho}_a \int_\Omega \boldsymbol{N_u^T N_{a,R}} d\Omega$

$\boldsymbol{K_s} = \bar{\rho}_s v^2 \int_\Omega \boldsymbol{N_u^T N_{u,RR}} d\Omega + \int_\Omega \boldsymbol{B_u^T D B_u} d\Omega$, $\boldsymbol{K_{sw}} = \bar{\rho}_w v^2 \int_\Omega \boldsymbol{N_u^T N_{w,RR}} d\Omega$,

$\boldsymbol{K_{sa}} = \bar{\rho}_a v^2 \int_\Omega \boldsymbol{N_u^T N_{a,RR}} d\Omega$, $\boldsymbol{Q} = \alpha S_r \int_\Omega \left(\nabla \cdot \boldsymbol{N_u^T}\right) \boldsymbol{N_p^w} d\Omega$,

$\boldsymbol{R} = \alpha(1 - S_r) \int_\Omega \left(\nabla \cdot \boldsymbol{N_u^T}\right) \boldsymbol{N_p^a} d\Omega$, $\boldsymbol{f^u} = \int_\Gamma \boldsymbol{N_u^T t_u} d\Gamma$

The momentum conservation equation for the pore water is discretized as (see Appendix A for full derivation):

$$\boldsymbol{M_{mw} \ddot{U}_w} + \boldsymbol{C_{mw}^s \dot{u}} + \boldsymbol{C_{mw} \dot{U}_w} + \boldsymbol{K_{mw}^s u} + \boldsymbol{K_{mw} U_w} + \boldsymbol{I_{mw} p^w} = \boldsymbol{f_{mw}} \tag{29}$$

Where the mass, damping and stiffness matrices are:

$\boldsymbol{M_{mw}} = -\rho_w \int_\Omega \boldsymbol{N_w^T N_w}\, d\Omega$, $\boldsymbol{C_{mw}^s} = \eta_w \int_\Omega \boldsymbol{N_w^T N_u}\, d\Omega$, $\boldsymbol{C_{mw}} = 2v\rho_w \int_\Omega \boldsymbol{N_w^T N_{w,R}} d\Omega - \eta_w \int_\Omega \boldsymbol{N_w^T N_w} d\Omega$, $\boldsymbol{K_{mw}^s} = -\eta_w v \int_\Omega \boldsymbol{N_w^T N_{u,R}}\, d\Omega$, $\boldsymbol{K_{mw}} = -\rho_w v^2 \int_\Omega \boldsymbol{N_w^T N_{w,RR}}\, d\Omega + \eta_w v \int_\Omega \boldsymbol{N_w^T N_{w,R}}$, $\boldsymbol{I_{mw}} = \int_\Omega \boldsymbol{N_{w,i}^T N_p^w} d\Omega$, $\boldsymbol{f_{mw}} = \int_\Gamma \boldsymbol{N_w^T} p_n^w d\Gamma$

The momentum conservation equation for the pore gas is discretized as (see Appendix A for derivation):

$$\boldsymbol{M_{ma} \ddot{U}_a} + \boldsymbol{C_{ma}^s \dot{u}} + \boldsymbol{C_{ma} \dot{U}_a} + \boldsymbol{K_{ma}^s u} + \boldsymbol{K_{ma} U_a} + \boldsymbol{I_{ma} p^a} = \boldsymbol{f_{ma}} \tag{30}$$

Where the mass, damping and stiffness matrices are:

$\boldsymbol{M_{ma}} = -\rho_a \int_\Omega \boldsymbol{N_a^T N_a}\, d\Omega$, $\boldsymbol{C_{ma}^s} = \eta_a \int_\Omega \boldsymbol{N_a^T N_u}\, d\Omega$, $\boldsymbol{C_{ma}} = 2v\rho_a \int_\Omega \boldsymbol{N_a^T N_{a,R}} d\Omega - \eta_a \int_\Omega \boldsymbol{N_a^T N_a} d\Omega$, $\boldsymbol{K_{ma}^s} = -\eta_a v \int_\Omega \boldsymbol{N_a^T N_{u,R}}\, d\Omega$, $\boldsymbol{K_{ma}} = -\rho_a v^2 \int_\Omega \boldsymbol{N_a^T N_{a,RR}}\, d\Omega + \eta_a v \int_\Omega \boldsymbol{N_a^T N_{a,R}}$, $\boldsymbol{I_{ma}} = \int_\Omega \boldsymbol{N_{a,i}^T N_p^a} d\Omega$, $\boldsymbol{f_{ma}} = \int_\Gamma \boldsymbol{N_a^T} p_n^a d\Gamma$

The mass conservation equation for the pore water is discretized as (see Appendix A for derivation):

$$\boldsymbol{C}_{qw}^{s}\dot{\boldsymbol{u}}+\boldsymbol{C}_{qw}\dot{\boldsymbol{U}}_{w}+\boldsymbol{H}_{qw}^{w}\dot{\boldsymbol{p}}^{w}+\boldsymbol{H}_{qw}^{a}\dot{\boldsymbol{p}}^{a}+\boldsymbol{K}_{qw}^{s}\boldsymbol{u}+\boldsymbol{K}_{qw}\boldsymbol{U}_{w}+\boldsymbol{Q}_{qw}^{w}\boldsymbol{p}^{w}+\boldsymbol{Q}_{qw}^{a}\boldsymbol{p}^{a}=\boldsymbol{f}_{qw} \tag{31}$$

Where the mass, damping and stiffness matrices are:

$\boldsymbol{C}_{qw}^{s}=\alpha S_r\int_{\Omega}\left(\boldsymbol{N}_{\boldsymbol{p}}^{w}\right)^{\boldsymbol{T}}\nabla\cdot\boldsymbol{N}_{\boldsymbol{u}}\,d\Omega+nS_r\int_{\Omega}\left(\nabla\boldsymbol{N}_{\boldsymbol{p}}^{w}\right)^{\boldsymbol{T}}\boldsymbol{N}_{\boldsymbol{u}}\,d\Omega,\ \ \boldsymbol{C}_{qw}=-nS_r\int_{\Omega}\left(\nabla\cdot\boldsymbol{N}_{\boldsymbol{p}}^{w}\right)^{\boldsymbol{T}}\boldsymbol{N}_{\boldsymbol{w}}d\Omega,$

$\boldsymbol{H}_{qw}^{w}=w_1\int_{\Omega}\left(\boldsymbol{N}_{\boldsymbol{p}}^{w}\right)^{\boldsymbol{T}}\boldsymbol{N}_{\boldsymbol{p}}^{w}d\Omega,\ \ \boldsymbol{H}_{qw}^{a}=w_2\int_{\Omega}\left(\boldsymbol{N}_{\boldsymbol{p}}^{w}\right)^{\boldsymbol{T}}\boldsymbol{N}_{\boldsymbol{p}}^{a}d\Omega,$

$\boldsymbol{K}_{qw}^{s}=-\alpha S_r v\int_{\Omega}\left(\boldsymbol{N}_{\boldsymbol{p}}^{w}\right)^{\boldsymbol{T}}\nabla\cdot\boldsymbol{N}_{\boldsymbol{u},\boldsymbol{R}}\,d\Omega-nS_r v\int_{\Omega}\left(\nabla\cdot\boldsymbol{N}_{\boldsymbol{p}}^{w}\right)^{\boldsymbol{T}}\boldsymbol{N}_{\boldsymbol{u},\boldsymbol{R}},\ \ \boldsymbol{K}_{qw}=nS_r v\int_{\Omega}\left(\nabla\cdot\boldsymbol{N}_{\boldsymbol{p}}^{w}\right)^{\boldsymbol{T}}\boldsymbol{N}_{\boldsymbol{w},\boldsymbol{R}},$

$\boldsymbol{Q}_{qw}^{w}=-vw_1\int_{\Omega}\left(\boldsymbol{N}_{\boldsymbol{p}}^{w}\right)^{\boldsymbol{T}}\boldsymbol{N}_{\boldsymbol{p},\boldsymbol{R}}^{w}\,d\Omega,\ \ \boldsymbol{Q}_{qw}^{a}=-vw_2\int_{\Omega}\left(\boldsymbol{N}_{\boldsymbol{p}}^{w}\right)^{\boldsymbol{T}}\boldsymbol{N}_{\boldsymbol{p},\boldsymbol{R}}^{a}\,d\Omega,$

$\boldsymbol{f}_{qw}=\int_{\Gamma}\left(\boldsymbol{N}_{\boldsymbol{p}}^{w}\right)^{\boldsymbol{T}}\boldsymbol{q}^{w}d\Gamma;$

Where $\boldsymbol{q}^{w}$ is the boundary flux for the pore water phase and $\boldsymbol{f}_{qw}$ is the equivalent load matrix. The mass conservation equation for the pore gas is discretized as (see Appendix A for derivation):

$$\boldsymbol{C}_{qa}^{s}\dot{\boldsymbol{u}}+\boldsymbol{C}_{qa}\dot{\boldsymbol{U}}_{a}+\boldsymbol{H}_{qa}^{w}\dot{\boldsymbol{p}}^{w}+\boldsymbol{H}_{qa}^{a}\dot{\boldsymbol{p}}^{a}+\boldsymbol{K}_{qa}^{s}\boldsymbol{u}+\boldsymbol{K}_{qa}\boldsymbol{U}_{a}+\boldsymbol{Q}_{qa}^{w}\boldsymbol{p}^{w}+\boldsymbol{Q}_{qa}^{a}\boldsymbol{p}^{a}=\boldsymbol{f}_{qa} \tag{32}$$

Where the mass, damping and stiffness matrices are:

$\boldsymbol{C}_{qa}^{s}=\alpha(1-S_r)\int_{\Omega}\left(\boldsymbol{N}_{\boldsymbol{p}}^{a}\right)^{\boldsymbol{T}}\nabla\cdot\boldsymbol{N}_{\boldsymbol{u}}\,d\Omega-n(1-S_r)\int_{\Omega}\left(\nabla\boldsymbol{N}_{\boldsymbol{p}}^{a}\right)^{\boldsymbol{T}}\boldsymbol{N}_{\boldsymbol{u}}\,d\Omega,$

$\boldsymbol{C}_{qa}=-n(1-S_r)\int_{\Omega}\left(\nabla\cdot\boldsymbol{N}_{\boldsymbol{p}}^{a}\right)^{\boldsymbol{T}}\boldsymbol{N}_{\boldsymbol{w}}d\Omega,$

$\boldsymbol{H}_{qa}^{w}=g_1\int_{\Omega}\left(\boldsymbol{N}_{\boldsymbol{p}}^{a}\right)^{\boldsymbol{T}}\boldsymbol{N}_{\boldsymbol{p}}^{w}d\Omega,\ \ \boldsymbol{H}_{qa}^{a}=g_2\int_{\Omega}\left(\boldsymbol{N}_{\boldsymbol{p}}^{a}\right)^{\boldsymbol{T}}\boldsymbol{N}_{\boldsymbol{p}}^{a}d\Omega,$

$\boldsymbol{K}_{qa}^{s}=-\alpha(1-S_r)v\int_{\Omega}\left(\boldsymbol{N}_{\boldsymbol{p}}^{a}\right)^{\boldsymbol{T}}\nabla\cdot\boldsymbol{N}_{\boldsymbol{u},\boldsymbol{R}}\,d\Omega-n(1-S_r)v\int_{\Omega}\left(\nabla\cdot\boldsymbol{N}_{\boldsymbol{p}}^{a}\right)^{\boldsymbol{T}}\boldsymbol{N}_{\boldsymbol{u},\boldsymbol{R}},$

$\boldsymbol{K}_{qa}=n(1-S_r)v\int_{\Omega}\left(\nabla\cdot\boldsymbol{N}_{\boldsymbol{p}}^{a}\right)^{\boldsymbol{T}}\boldsymbol{N}_{\boldsymbol{a},\boldsymbol{R}},$

$\boldsymbol{Q}_{qa}^{w}=-vg_1\int_{\Omega}\left(\boldsymbol{N}_{\boldsymbol{p}}^{a}\right)^{\boldsymbol{T}}\boldsymbol{N}_{\boldsymbol{p},\boldsymbol{R}}^{w}\,d\Omega,\ \ \boldsymbol{Q}_{qa}^{a}=-vg_2\int_{\Omega}\left(\boldsymbol{N}_{\boldsymbol{p}}^{a}\right)^{\boldsymbol{T}}\boldsymbol{N}_{\boldsymbol{p},\boldsymbol{R}}^{a}\,d\Omega,$

$\boldsymbol{f}_{qa}=\int_{\Gamma}\left(\boldsymbol{N}_{\boldsymbol{p}}^{a}\right)^{\boldsymbol{T}}\boldsymbol{q}^{a}d\Gamma;$

and $\boldsymbol{q}^{a}$ is the boundary flux for the pore gas phase and $\boldsymbol{f}_{qa}$ is the equivalent load matrix.

3.3 Boundary conditions

The dynamic governing equations for unsaturated trackbed are transformed into the moving mixed element form using the equivalent weak-form integral of the momentum conservation, mass conservation, and constitutive equations. The natural boundary conditions for the seepage boundary and the stress boundary can also be determined in the same weak form manner.

$$n_j nS_r((\dot{u}_i^{w}-vu_{i,R}^{w})-(\dot{u}_i^{s}-vu_{i,R}^{s}))=\dot{W}_n \tag{33}$$

$$n_j n(1-S_r)((\dot{u}_i^{a}-vu_{i,R}^{a})-(\dot{u}_i^{s}-vu_{i,R}^{s}))=\dot{V}_n \tag{34}$$

$$n_j(\sigma_{ij}'-\alpha S_r p^{w}-\alpha(1-S_r)p^{a})=t_i \quad \text{on } \Gamma_t \tag{35}$$

In order to maintain continuity within the solution domain, the model must satisfy the continuity condition for displacement and stress.

$$u = u_0 \tag{36}$$

$$\sigma = \sigma_0 \tag{37}$$

3.4 Galerkin stabilization

The traditional Galerkin method is effective in handling conventional wave problems without numerical oscillations. However, when dealing with the diffusion equation, the Galerkin method can exhibit significant numerical oscillations and lead to a loss of accuracy when the gradient undergoes large changes. To mitigate computational uncertainties, it is necessary for the multi-field coupled variables to satisfy the Ladyzhenskaya-Babuska-Brezzi (LBB) [42] condition, which requires the displacement element to be at least one order higher than the pore-pressure element. The element form shown in Fig. 5 satisfies the LBB condition, with a 9-node Lagrange-second-order form for the displacement element and a 4-node Lagrange-first-order form for the pore pressure element.

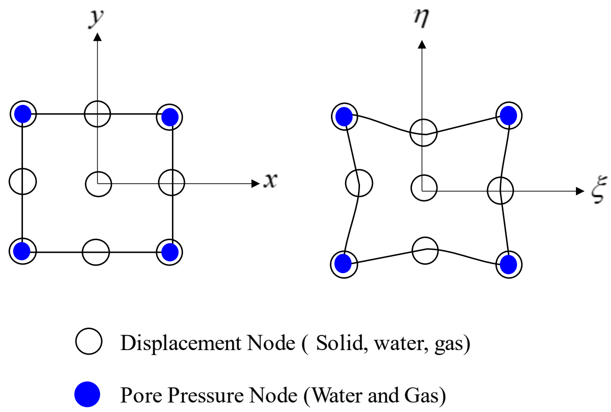

Fig. 5 Discretization of mixed element under the LBB condition

To evaluate the efficacy of the stabilized method, an approximately saturated soil is chosen as the subject of an analysis. The model's calculation parameters are set as follows: $E = 1.8GPa, \rho_s = 2400kg/m^3, \rho_w = 1000kg/m^3, v = 0.3, K_w = 2.2GPa, n = 0.15, k = 10^{-13}, S_r = 0.9999$. The elastic trackbed's calculation parameters are as follows: $\rho_d = 2300kg/m^3, E = 1.3GPa, v = 0.2$. The magnitude of the moving load is $F = 700kPa$ and the moving speed is $v = 15m/s$. The stability of the solution method is assessed by analyzing the time-curves of observation points located in the middle of the pavement.

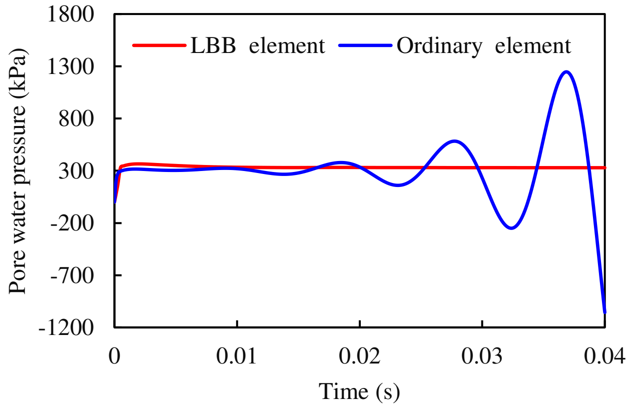

Fig. 6 Comparison between the LBB stabilization method and the non-stabilization method

In Fig. 6, it is evident that the moving mixed element method (MMEM) without the stabilized technique presents numerical instability in the dynamic response. Specifically, the pore water pressure (PWP) does not reach a steady state. The numerical test results demonstrate stability when the displacements of the solid and fluid phases are one order higher than the pore fluid pressure. No numerical oscillation issues arise in this case. Thus, the LBB technique is employed in all subsequent analyses.

4 Validation and comparison

Currently, there is a limited amount of field test data available considering trackbed dynamics with varying levels of moisture content. Therefore, to assess the accuracy of the proposed model, a multi-step verification process is conducted. First, the accuracy of the vehicle-track-elastic trackbed coupling system is verified. Building on this, the accuracy of the calculation method for the proposed unsaturated trackbed model is then assessed.

4.1 Validation 1: Vehicle-track-trackbed coupling system

For solely checking the vehicle-track coupling, the trackbed is considered elastic and a comparison is made with the calculation results of Li et al. [43], as illustrated in Fig. 7. The high-speed train is a CRH3-EMU operated at a speed of 72 km/h and the track structure is a CRTS-II ballastless track.

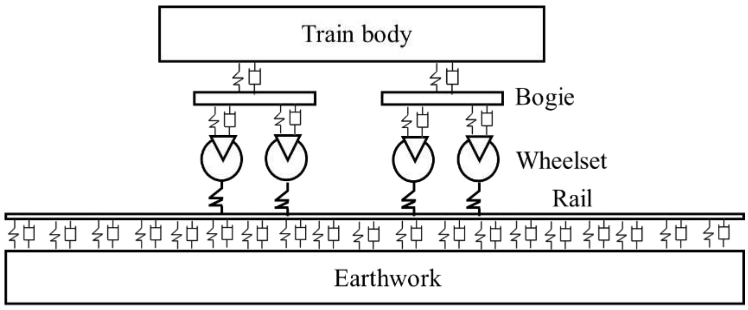

Fig. 7 Vehicle-track-trackbed coupling calculation model

In Fig. 8, the results obtained are shown to be in agreement with those obtained from the literature. The dynamic interaction force between the wheel and rail, as well as the displacement of the rail surface, show strong correlation with those calculated by Li et al. [43].

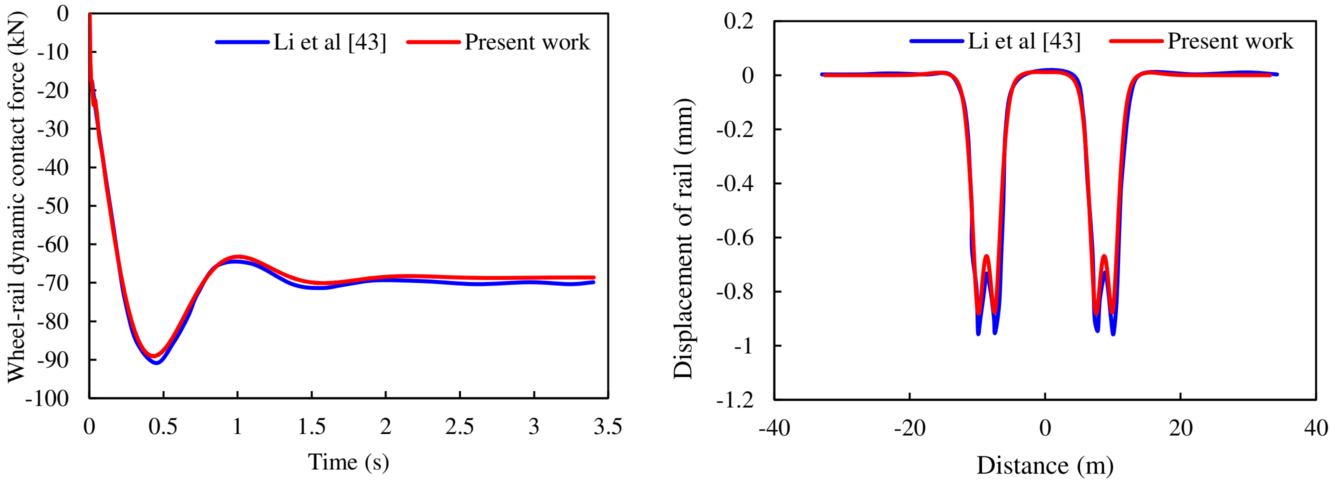

(a) Wheel-rail contact force (b) Displacement of rail

Fig. 8 Comparison of vehicle-track coupling models

4.2 Validation 2: Unsaturated foundation dynamics

The unsaturated dynamics model was validated using the results presented in Xu [39] as illustrated in Fig. 9. To do so, the unsaturated foundation is modeled using a 3D domain, with a depth of 20 m and 10 m width and length. The loading area is within $-0.5m \leq x \leq 0.5m$ and $-0.5m \leq y \leq 0.5m$. It is a stationary harmonic load $q(x,y)e^{i\omega t}$ with an amplitude of $1kN/m^2$ and a frequency of $\omega = 1Hz$. The surface of the unsaturated foundation is permeable, while the base is fixed. No lateral displacement occurs on the sides, and the mesh size is 0.1m.

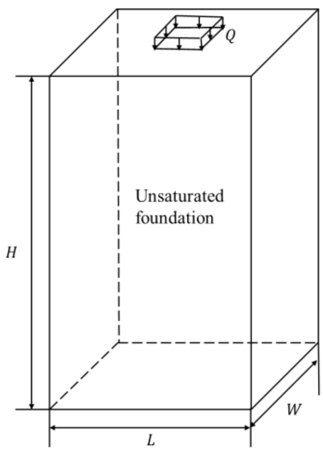

Fig. 9 Calculation model of unsaturated foundation

Fig. 10 demonstrates excellent agreement between the present results and the analytical method from the literature. This confirms that the proposed multi-field coupling model can accurately calculate the pore pressures and total stresses in unsaturated foundations.

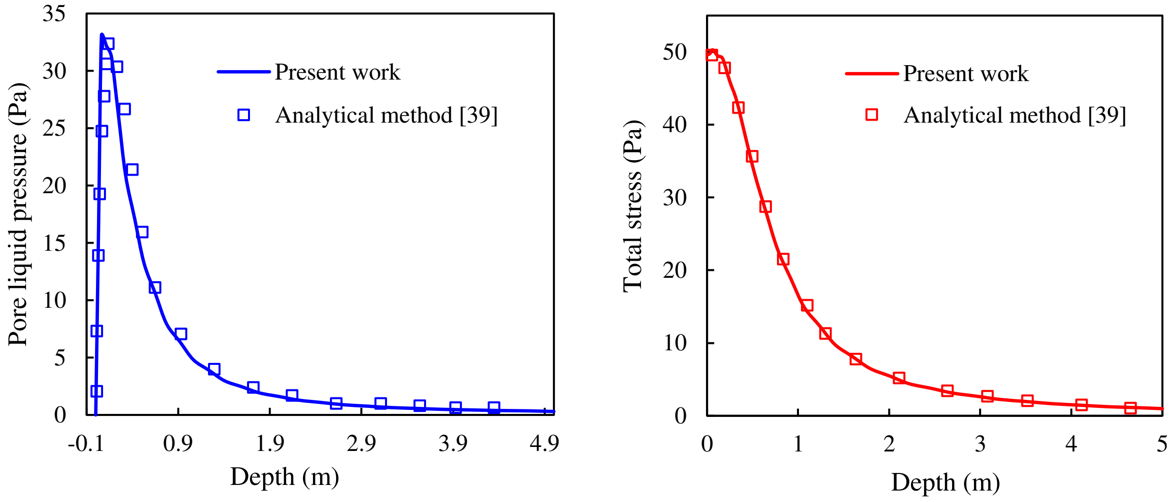

(a) Pore liquid pressure (b) Total stress

Fig. 10 Comparison of vibration of unsaturated foundation ($\boldsymbol{S_r = 0.9}$)

4.3 Validation 3: Saturated foundation with moving load

A saturated porous medium is a sub-case of an unsaturated porous medium model, representing a solution when the saturation degree approaches 1 ($S_r \to 1$). To assess the stability and accuracy of the dynamic model for unsaturated porous media, Ye et al. [44] and Zhang et al. [45] employed saturated porous medium to validate the dynamic response outcomes for unsaturated soil. The computational parameters for the saturated porous medium are as follows [46]: $\rho_s = 1816 kg/m^3$, $G = 10^8 Pa$, $K_w = 2.45 \times 10^9 Pa$, $\bar{k} = 10^{-7} m^3\, s/kg$. The moving load has a speed of 20 m/s, while the degree of saturation is 0.99999. The saturated foundation has a thickness of 18 m, a length of 100 m, and a mesh size of 0.5 m, as illustrated in Fig. 11.

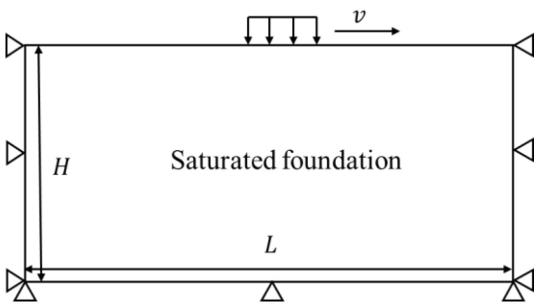

Fig. 11 Calculation model of saturated foundation

Fig. 12 compares the proposed method with the solution calculated in [46]. A strong match between effective vertical stress is evident. This demonstrates the applicability of the proposed moving mixed element method for saturated problems subject to moving loads.

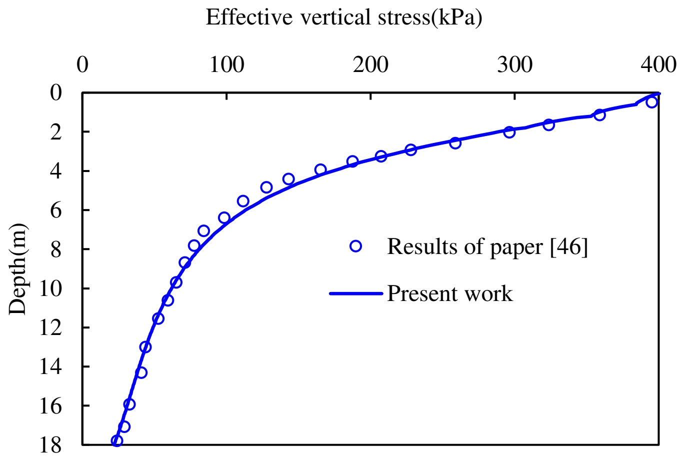

Fig. 12 Comparison of calculation results of saturated foundation

5 Analysis

An analysis is first performed to investigate the general behavior of an unsaturated trackbed. This is then followed by investigation into the degree of saturation, train speed and track irregularities. The architecture of the model is illustrated in Fig. 3, considering the excitation of a CRH380-EMU high-speed train shown in Table 2 [47], running onthe CRTS-II ballastless track shown in Table 3. The calculation parameters for all earthworks are given in Table 1. The analysis model has a length of 100 m in the train passage direction, which aims to minimise the error caused by boundary reflections. [36]. The element mesh size is 0.1 m. simulations were executed on a high-performance computing workstation featuring a 13th-generation Intel(R) Core(TM) i9-13900K processor and 128 GB ofRAM.

Table 2 Vehicle parameters of CRH380-EMU

Parameters	Values
Train body mass (kg)	4000
Bogie mass (kg)	3200
Wheelset mass (kg)	2400
Train body pitch moment of inertia $(kg \cdot m^2)$	5.47×10^5
Bogie pitch moment of inertia $(kg \cdot m^2)$	6800
Primary suspension stiffness (N/m)	2.08×10^6
Primary suspension damping $(N \cdot s/m)$	1.00×10^5
Secondary suspension stiffness (N/m)	0.8×10^6
Secondary suspension damping $(N \cdot s/m)$	1.20×10^5
Bogie distance (m)	17.5
Wheel distance (m)	2.5
Wheel rolling radius (m)	0.457

Table 3 CRTS II ballastless track parameters

Parameters	Values

Rail (kg/m)	60
Rail stiffness $(\mathrm{kN.m^2})$	6756
Fastener stiffness $(\mathrm{kN/m})$	60
Fastener damping $(\mathrm{MN.s/m})$	47.7
Density of track slab $(\mathrm{kg/m^3})$	2500
Elastic modulus of track slab (MPa)	36000
Poisson's ratio of track slab $(N \cdot s/m)$	0.2
CA mortar stiffness $(\mathrm{MN/m})$	900
CA mortar damping $(\mathrm{kN.s/m})$	83
Density of concrete base $(\mathrm{kg/m^3})$	2500
Elastic modulus of concrete base (MPa)	34000
Poisson's ratio of concrete base	0.2

5.1 General analysis

To investigate the dynamic behavior of an unsaturated trackbed under train loading, a dimensionless parameter, $S_r = 0.95$, serves as the object of research in order to analyze the disparity between the transient and steady-state responses of an unsaturated trackbed . Table 1-3 lists all other calculation parameters. The observation point is located at the midpoint of the trackbed in the vertical direction. It is worth noting that the computation time for analyzing the vehicle-track-unsaturated trackbed using FEM is 4,732 s, whereas the MMEM approach only requires 275 s. Thus, the computation time for FEM is 17.21 times longer than that of MMEM.

Fig. 13 displays the initial time-history curves of PWP and vertical displacement (VD) showing that they oscillate before reaching their steady state after approximately 2 seconds. The dynamic response of the trackbed to a high-speed train is a result of the interaction of stress waves within the trackbed, eventually reaching a steady-state condition. The steady-state DPWP reaches 351 Pa while the steady-state VD is -0.16 mm.

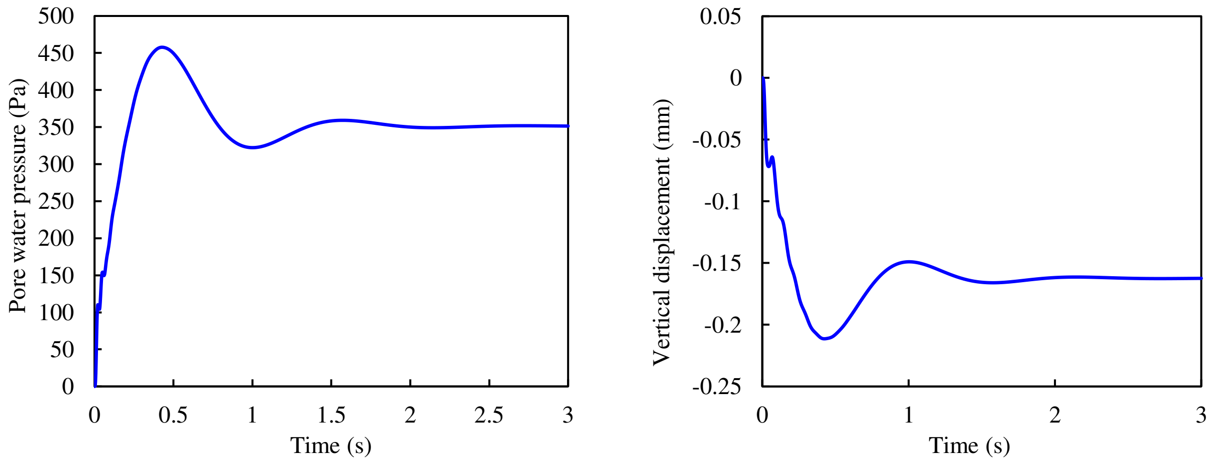

(a) (b)

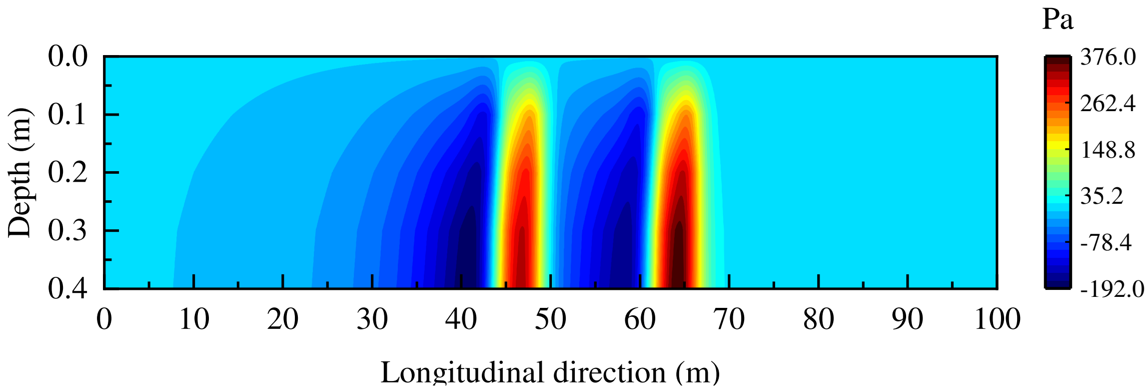

(c)

Fig. 13 Time-varying characteristics of dynamic response of unsaturated trackbed, (a) Pore water pressure, (b) Vertical displacement, (c) Pore water pressure distribution at steady state

Fig. 13(c) illustrates the distribution of PWP in the unsaturated trackbed of the ballastless track at 3s. At this point, the system has entered a steady state and the hydraulic gradient of the unsaturated trackbed is from the bottom to the top in the vertical direction. Additionally, a noticeable negative pore water pressure region is formed between the two bogies of the high-speed train. The maximum pore water pressure gradient (maximum positive pore pressure to maximum negative pore pressure) created by the first bogie of a high-speed train can cover an area of about 7.5 m. The second bogie creates a wider range of pore water pressure fluctuations.

5.2 Effect of degree of saturation

When cracks occur in a ballastless track, rainwater infiltrates the trackbed, leading to changes in moisture content. For example, depending upon clay content, this can cause it to transition from a desiccated to a saturated state. Therefore, it is important to evaluate the hydro-mechanical response under varying degrees of saturation. To do so the train speed is set to 300 km/h ($v = 300\ km/h$) and the rails are considered perfectly smooth. The steady-state distribution of PWP and VD inside the trackbed below the first bogie is analysed. Fig. 14**Error! Reference source not found.** (a) illustrates the distribution of PWP within the unsaturated trackbed. At a degree of saturation of 0.99, the maximum PWP is 1.57 kPa, located in the middle of the trackbed. At degrees of saturation of 0.95 and 0.9, the PWP is better distributed, with values of 382 Pa and 190.51 Pa respectively. Increasing the degree of saturation from 0.9 to 0.95 results in an average increase of 100.51% in the PWP. Similarly, as the degree of saturation increases from 0.95 to 0.99, the PWP increases by 310.10%.

VD is important for the smooth operation of high-speed trains. Therefore, it's essential to evaluate its impact on quasi-static deflection, especially when rainwater infiltrates the interior of the trackbed. As displayed in Fig. 14**Error! Reference source not found.** (b), the VD of the trackbed under varying degrees of saturation is evident. Increasing the degree of saturation from 0.9 to 0.95 results in a mere 0.16% increase in VD. However, VD shows a greater increase of 0.97% when the degree of saturation rises from 0.95 to 0.99, compared to the increase of 0.9 to 0.95. Although the process of increasing water content has a minimal impact on quasi-static VD, it should be noted that it creates a hydraulic gradient that can gradually lead to the depletion of fine particles within the trackbed. This depletion can damage the trackbed, reducing its durability and intensifying the occurrence of cracks.

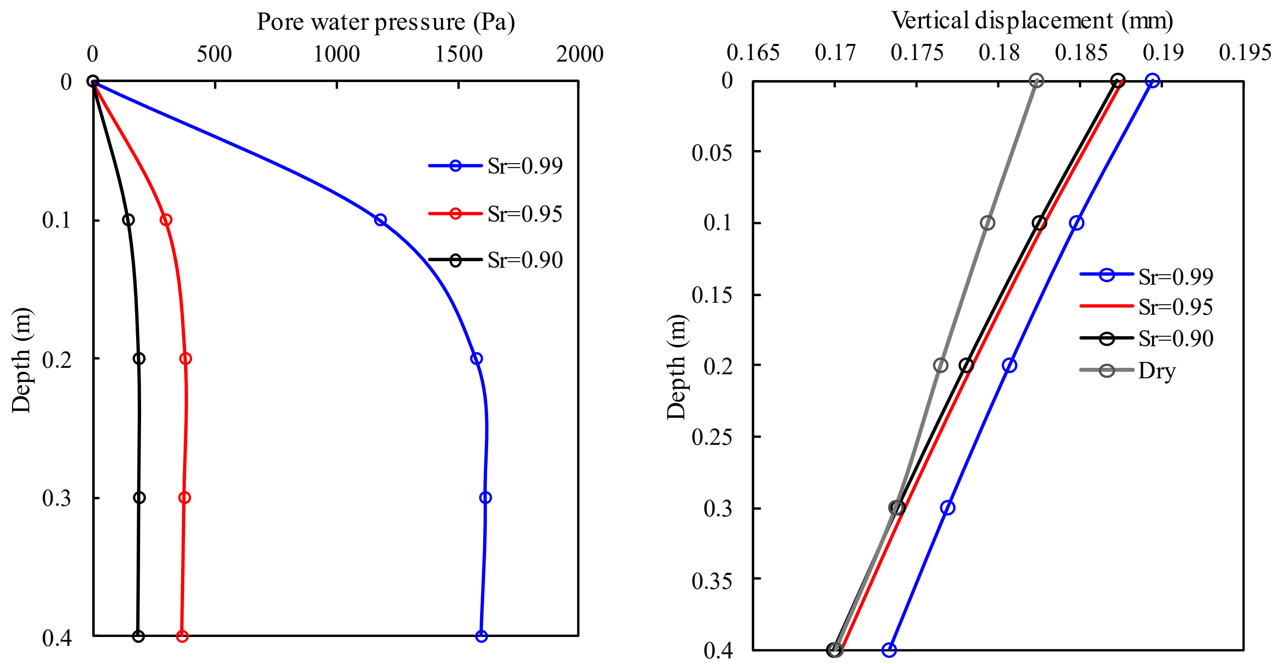

(a) (b)

Fig. 14 The effect of the degree of saturation on the index of hydrodynamic response, (a) Pore water pressure, (b) Vertical displacement

5.3 Effect of train speed

According to the International Union of Railways (UIC), a high-speed railway is defined as having trains that operate at speeds exceeding 200 km/h. The operating velocity of trains can impact the dynamic response of the trackbed [48, 49]. To evaluate the amplification of quasi-static unsaturated trackbed deflection with speed, the degree of saturation (S_r) is set to 0.9 and rail irregularity is ignored.

Fig. 15 (a) illustrates the distribution of PWP in the unsaturated trackbed at various speeds. At a train velocity of 450 km/h, the PWP inside the trackbed is 207.32 Pa, concentrated in the middle section. At train velocities of 350 km/h and 250 km/h, the PWP inside the trackbed is 197.40 Pa and 182.76 Pa, respectively. Upon observing the trend of PWP within the trackbed, it's evident that the pressure increases rapidly from the trackbed's surface, while the growth rate of PWP experiences a rapid decrease at a depth of 0.1 m. Below a depth of 0.2 m, the PWP shows a decreasing trend. The maximum PWP increases by 8.01% and 13.44% as the train velocity increases from 250 km/h to 450 km/h, respectively. Furthermore, at different velocities ($V = 450\ km/h \rightarrow 250\ km/h$), the PWP decreases from the middle to the bottom of the trackbed by 8.70%, 4.62%, and 1.22%, respectively.

As the train velocity increases, the unevenness of PWP within the trackbed becomes more pronounced. Conversely, when the train velocity is reduced to 250 km/h, the distribution of PWP gradually becomes more uniform. The distribution of PWP within the trackbed varies with different degrees of saturation, resulting in non-uniformity. Consequently, this uneven distribution of particle gradation in the trackbed soil significantly impacts its compactness.

Fig. 15 (b) presents VD as the train velocity increases. VD exhibits an approximately linear distribution. The maximum VD is 0.205 mm when the train velocity increases from 250 km/h to 450 km/h. The increase in maximum VD fluctuates by 4.35% and 11.41%, respectively. In contrast to the dry trackbed, the displacements are all higher in the wet trackbed than in the dry, and the higher the train speed, the greater this difference.

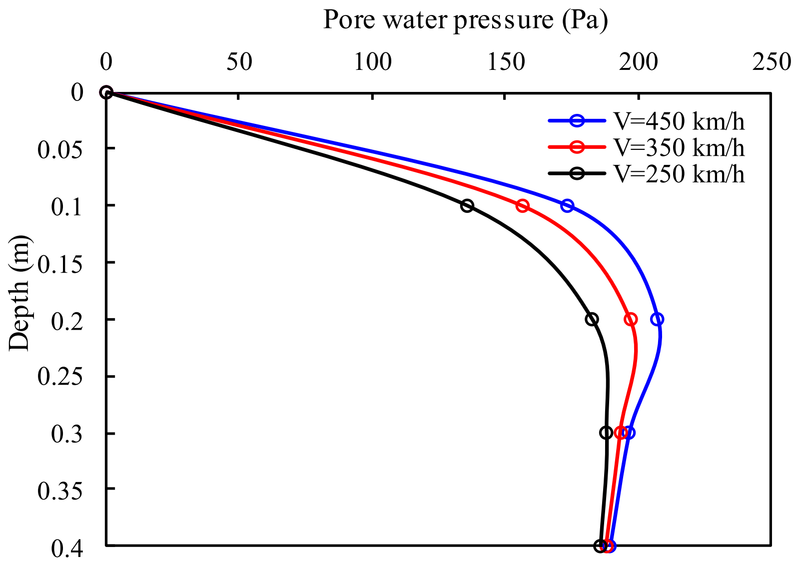

(a)

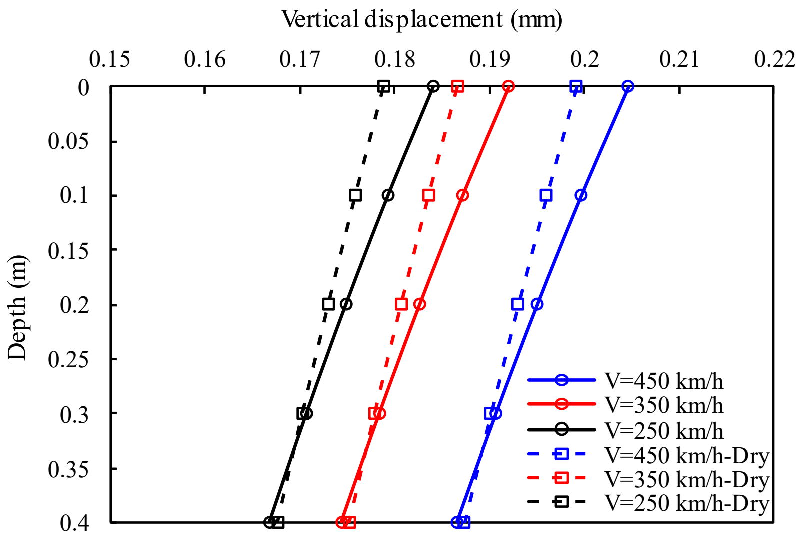

(b)

Fig. 15 Effect of train speed on hydrodynamic response of an unsaturated trackbed, (a) The distribution of pore water pressure, (b) The distribution of displacement

Fig. 16(a) shows the maximum displacement of the rail surface at different speeds in terms of distance, with the four corresponding to the axles of the train. At the wheel loading position, the deformation of the rail gradually becomes larger as the train speed increases (e.g. the maximum displacement at 450km/h is 5.7% higher than that at 250km/h). As shown in Fig.

16(b), the displacement of the rail surface is marginally higher when there is a presence of water in the trackbed.

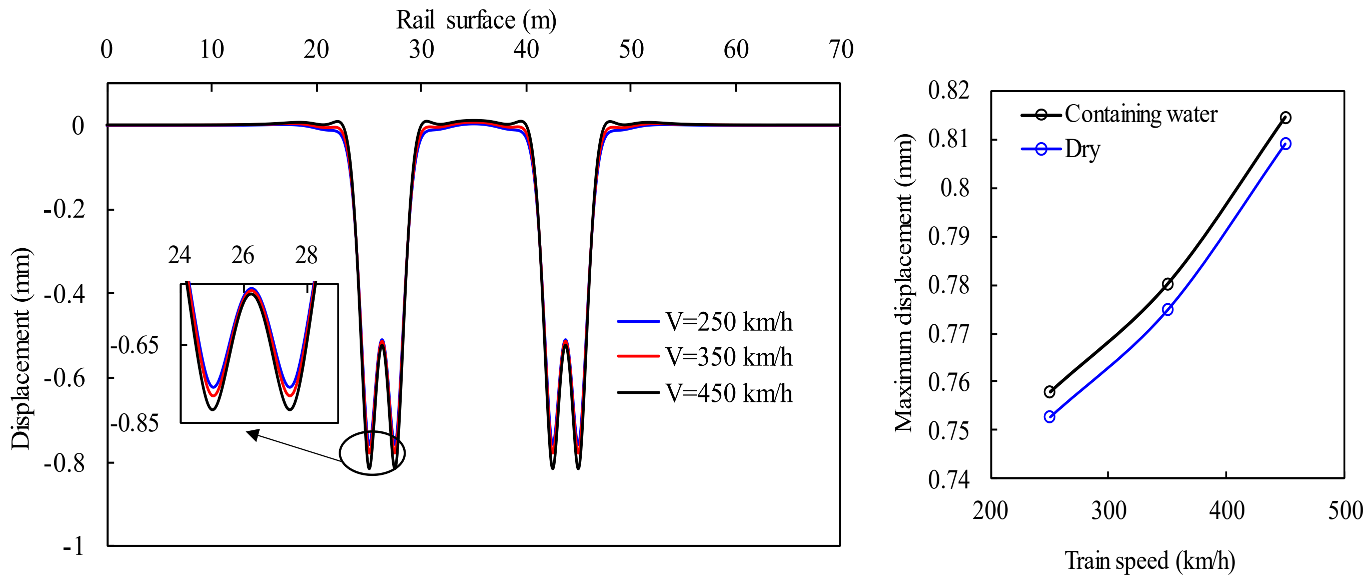

(a). (b)

Fig. 16 The effect of speed on rail displacement, (a) The distribution of rail displacement, (b) Maximum displacement of rails

5.4 Effect of track irregularities

Track irregularity is an important factor contributing to the variation in wheel-rail contact force. Over time, construction tolerances and the differential settlement of trackbed can lead to increased track irregularities, which in turn cause higher wheel-rail interaction forces. Therefore, it is important to analyze how track irregularities affect the hydromechanical response of unsaturated trackbeds.

To do so the speed of the high-speed train was set to 300 km/h and the degree of saturation of the trackbed was set to 0.9. It was assumed the track irregularities on the surface of the rails followed a simple harmonic pattern [50]. Using the notation in Fig. **17**, the rails were tested under two different conditions:

(1) The amplitude of the wave was considered constant ($A = 10mm$), and the wavelengths analyzed were $\lambda = 10m, 15mm, 20m$.

(2) The wavelength of the wave was considered constant ($\lambda = 10m$), and the different wave amplitudes analyzed were $A = 10mm, 5mm, 1mm$.

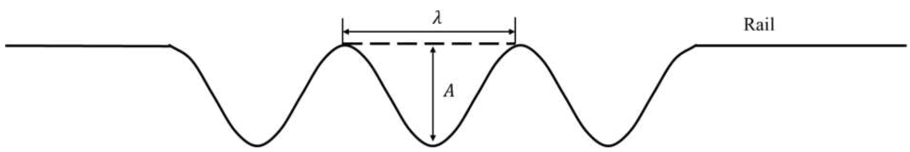

Fig. 17 Example rail irregularity

Fig. 18 illustrates the time-history variations of PWP and VD at the trackbed center. Fig. 18(a) displays the PWP under varying conditions of $\lambda = 10m$ and $= 10mm, 5mm$, and $1mm$. The average value of the PWP across the three different wave amplitude conditions is 190 Pa. At an amplitude of 10mm ($A = 10mm$), the maximum positive pore water pressure is 244.74 Pa, while the minimum value is 136.08 Pa. The peak PWP reaches 1.29 times the average value, representing an increase of approximately 29% from the maximum value. The minimum value is reduced by approximately 29% as well. The average VD is 0.178 mm, with a maximum value of 0.228 mm and a minimum value of 0.127 mm, indicating a variation of 28%.

When the irregularity amplitude is 5 mm ($A = 5\ mm$), the PWP ranges from 163.28 Pa to 217.61 Pa, with a fluctuation of 14.5%. Similarly, the VD varies from 0.152 mm to 0.205 mm, with a variation of 15.2%. When the amplitude decreases to 1 mm ($A = 1\ mm$), both the PWP and VD show minimal changes. The magnitudes of the PWP range from 185.01 Pa to 195.92 Pa, with an average fluctuation of 3%. The corresponding VD ranges from 0.173 mm to 0.183 mm, with an average fluctuation of 2.8%.

When the wavelength is kept constant, the amplitude of the irregularity is observed to increase from 1 mm to 10 mm. This increase leads to higher PWP, which rises by 3%, 14.5%, and 29% compared to the average value. However, the increase in VD follows a similar pattern and can be considered approximately linear.

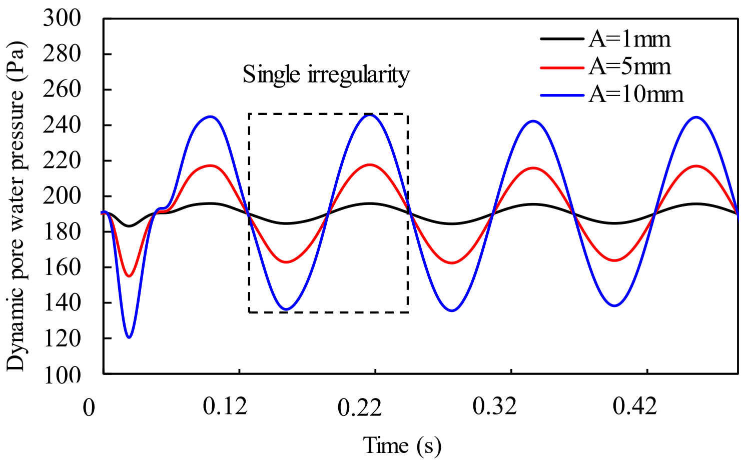

(a)

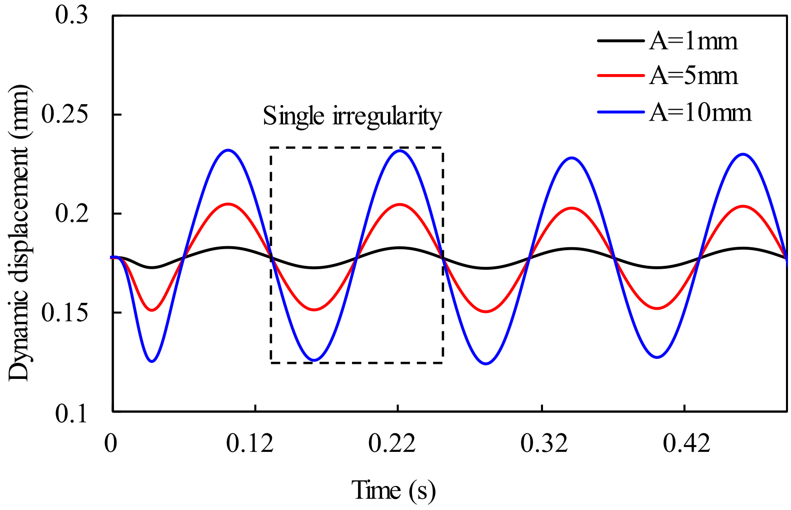

(b)

Fig. 18 The amplitude of track irregularities, (a) Pore water pressure, (b) Vertical displacement

The effects of irregularity wavelengths on the PWP and VD of an unsaturated trackbed of a ballastless track are shown in Fig. 19. Fig. 19 (a) and (b) illustrate the time-curves of PWP and VD for various wavelengths ($A = 10\ mm$ and $\lambda = 10\ m, 15\ m, 20\ m$). The average values of PWP and VD are 190.72 Pa and 0.178 mm, respectively. For a wavelength of 15 m ($\lambda = 15\ m$), the maximums and minimums of PWP are 219.40 Pa and 164.02 Pa, respectively, while the maximums and minimums of VD are 0.202 mm and 0.153 mm, respectively. These values indicate fluctuations of 14.52% and 13.76% relative to the average values. With a wavelength of 20 m ($\lambda = 20\ m$), the maximums and minimums of PWP are 206.66 Pa and 173.21 Pa, respectively, and the maximums and minimums of VD are 0.194 mm and 0.164 mm, respectively. The average fluctuations of PWP and VD are 8.77% and 8.42%, respectively.

The fluctuations in PWP, relative to the average value, are 29%, 14.52%, and 8.77% when the wavelength of track irregularity is increased from 10 m to 20 m. Furthermore, the variation of VD, relative to the average VD, is 28%, 13.76%, and 8.42%, respectively.

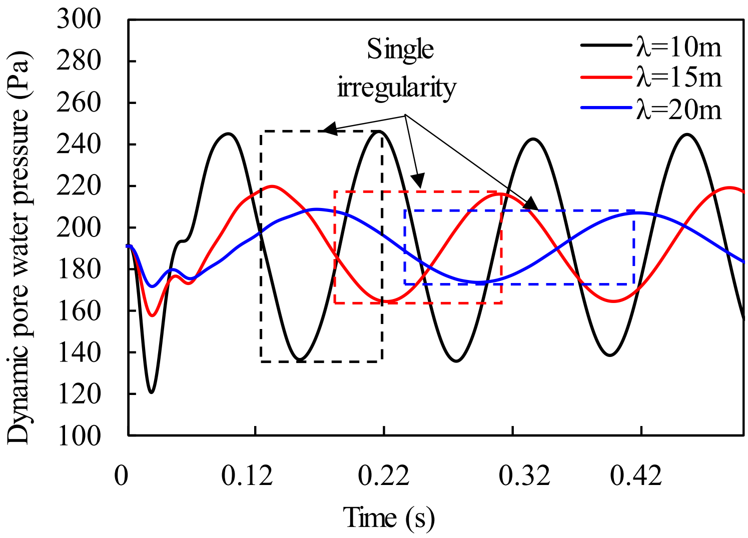

(a)

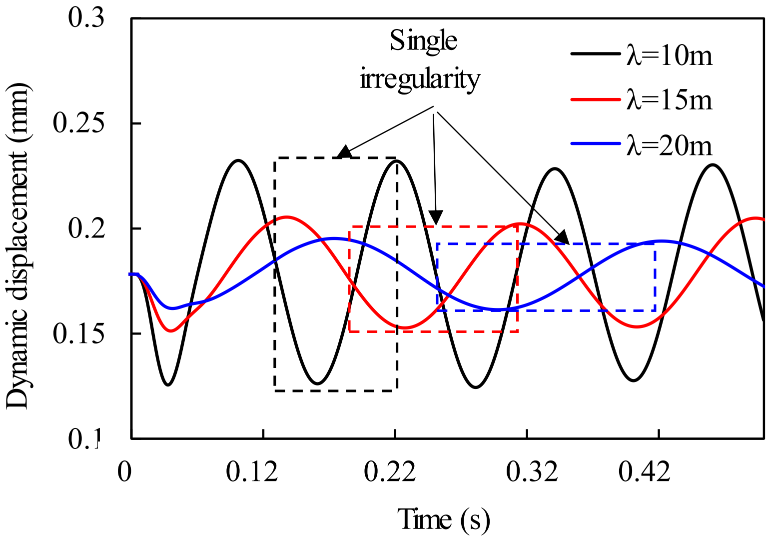

(b)

Fig. 19 The wavelength of track irregularities, (a) Pore water pressure, (b) Vertical displacement

The analysis results of the wavelength and amplitude of track irregularities demonstrate that these irregularities have a substantial impact on the internal hydraulic behavior of unsaturated trackbeds. Track irregularities result in a rapid increase in PWP.

6 Conclusions

Ballastless track is typically formed from concrete, which in the long-term, experiences cracking due to repeated train and thermal loading. Rainwater infiltrates the trackbed through ballastless track cracks leading to changes in the degree of saturation within the trackbed and underlying earthworks. To study this, a fully-coupled train-track-ground model considering multi-field coupling theory for a porous medium is developed. The moving mixed element method was developed based on the principle of relative motion and used to minimize computational requirements. Furthermore, a stabilization method was employed to prevent numerical oscillations. The accuracy of the model was validated through three numerical examples. The main conclusions were:

1. ~~The PWP inside the unsaturated trackbed initially reaches a maximum value when the moving force is applied and then quickly decays to the steady-state value. When the degree of saturation of trackbed is 0.95, the stable PWP is approximately 351 Pa and the steady-state VD is -0.16 mm. The maximum pore water pressure gradient created by the first bogie of a high-speed train can cover an area of about 7.5 m.~~
2. When the wavelength remains constant, increasing the rail irregularity amplitude from 1 mm to 10 mm results in variations in PWP of 3%, 14.5%, and 29% compared to the average value. Similarly, the increase in VD shows a nearly linear pattern. Conversely, when the amplitude of the wave is constant and the wavelength of the track irregularity is increased from 10 m to 20 m, PWP changes by 29%, 14.52%, and 8.77% relative to the average value. The corresponding variations in VD relative to the average displacement are 28%, 13.76%, and 8.42%.
3. Increasing the degree of saturation from 0.9 to 0.95 results in PWP increasing by 100%. Furthermore, increasing the degree of saturation from 0.95 to 0.99 results in PWP increasing by 310%. VD changes by only 0.16% when the degree of saturation increases from 0.9 to 0.95. An increase in the degree of saturation from 0.95 to 0.99 leads to a VD increase of 0.97%.
4. Increasing the train velocity from 250 km/h to 450 km/h results in maximum PWP increases of 8.01% and 13.44%, respectively. At different velocities ($V = 450\ km/h \rightarrow 250\ km/h$), PWP shows a decrease from the middle to the bottom of the trackbed, with reductions of 8.70%, 4.62%, and 1.22% observed. The maximum DD increases by 4.35% and 11.41% when the train velocity is increased from 250 km/h to 450 km/h, with a maximum displacement value of 0.205 mm. The rail maximum displacement at 450km/h is 5.7% higher than that at 250km/h.

Acknowledgement

The research was supported by National Natural Science Foundation of China (Grant No. 52078427 and 51978588); Joint Fund for Basic Railway Research (Grant No. U2268213); The authors gratefully acknowledge their financial support.

Appendix A Derivation of unsaturated trackbed matrix

By multiplying equation (24) with the test function $\boldsymbol{\delta u_i}$ simultaneously, the original partial differential equation is transformed into its corresponding equivalent integral weak form.

$$\begin{aligned}
\int_\Omega \sigma'_{ij,j}\delta u_i d\Omega - \int_\Omega \alpha S_r p^w_{,j}\delta u_i d\Omega - \int_\Omega \alpha(1-S_r)p^a_{,j}\delta u_i d\Omega \\
= \int_\Omega (\bar{\rho}_s \ddot{u}^s_i - 2v\bar{\rho}_s \dot{u}^s_{i,R} + \bar{\rho}_s v^2 u^s_{i,RR})\delta u_i d\Omega + \int_\Omega (\bar{\rho}_w \ddot{u}^w_i - 2v\bar{\rho}_w \dot{u}^w_{i,R} + \bar{\rho}_w v^2 u^w_{i,RR})\delta u_i d\Omega \\
+ \int_\Omega (\bar{\rho}_a \ddot{u}^a_i - 2v\bar{\rho}_a \dot{u}^a_{i,R} + \bar{\rho}_a v^2 u^a_{i,RR})\delta u_i d\Omega
\end{aligned}$$

Where the various sub-sections expand in the form of the following:

$$\int_\Gamma \delta u_i n_j(\sigma'_{ij} - \alpha S_r p^w - \alpha(1-S_r)p^a)d\Gamma$$

$$= \int_\Omega \delta u_{i,j}\left(\sigma'_{ij} - \alpha S_r p^w - \alpha(1-S_r)p^a\right)d\Omega + \int_\Omega (\bar{\rho}_s \ddot{u}_i^s - 2v\bar{\rho}_s \dot{u}_{i,R}^s + \bar{\rho}_s v^2 u_{i,RR}^s)\delta u_i d\Omega$$

$$+ \int_\Omega (\bar{\rho}_w \ddot{u}_i^w - 2v\bar{\rho}_w \dot{u}_{i,R}^w + \bar{\rho}_w v^2 u_{i,RR}^w)\delta u_i d\Omega + \int_\Omega (\bar{\rho}_a \ddot{u}_i^a - 2v\bar{\rho}_a \dot{u}_{i,R}^a + \bar{\rho}_a v^2 u_{i,RR}^a)\delta u_i d\Omega$$

The overall equation of motion for the trackbed structure can be expressed in a discrete format.

The test function $\delta \boldsymbol{u^w}$ is multiplied by both sides of the momentum conservation equation for pore water (25) in order to derive its equivalent integral weak form. This form is then obtained after integration by parts.

$$\int_\Omega \delta \boldsymbol{u}^{\boldsymbol{w}}_{,\boldsymbol{i}}\, p^w d\Omega - \int_\Omega \delta \boldsymbol{u^w} \rho_w\left(\ddot{u}_i^w - 2v\dot{u}_{i,R}^w + v^2 u_{i,RR}^w\right)d\Omega - \int_\Omega \delta \boldsymbol{u^w} \eta_w\left(\dot{u}_i^w - v u_{i,R}^w\right)d\Omega + \int_\Omega \delta \boldsymbol{u^w} \eta_w\left(\dot{u}_i^s - v u_{i,R}^s\right)d\Omega$$

$$= \int_\Gamma \delta \boldsymbol{u^w} n_i\, p^w d\Gamma$$

The momentum conservation equation for pore water can be expressed in a discrete format.

Multiplying both sides of the momentum conservation equation for pore gas (26) by the test function $\delta \boldsymbol{u^a}$ yields its equivalent integral weak form. After performing integration by parts, the following form is obtained.

$$\int_\Omega \delta \boldsymbol{u}^{\boldsymbol{a}}_{,\boldsymbol{i}}\, p^a d\Omega - \int_\Omega \delta \boldsymbol{u^a} \rho_a\left(\ddot{u}_i^a - 2v\dot{u}_{i,R}^a + v^2 u_{i,RR}^a\right)d\Omega - \int_\Omega \delta \boldsymbol{u^a} \eta_a\left(\dot{u}_i^a - v u_{i,R}^a\right)d\Omega + \int_\Omega \delta \boldsymbol{u^a} \eta_a\left(\dot{u}_i^s - v u_{i,R}^s\right)d\Omega$$

$$= \int_\Gamma \delta \boldsymbol{u^a} n_i\, p^a d\Gamma$$

The momentum conservation equation for pore gas can be expressed in a discrete format.

By multiplying both sides of equation (19), the mass conservation equation for pore water, with the test function $\boldsymbol{\delta p^w}$, its equivalent integral weak form is derived. Integration by parts leads to the following form.

$$nS_r \int_\Omega \delta p^w\left[\left(\dot{u}_{i,i}^w - v\nabla u_{i,R}^w\right) - \left(\dot{u}_{i,i}^s - v\nabla u_{i,R}^s\right)\right]d\Omega$$

$$= -nS_r \int_\Omega \delta p^w_{,i}\left(\dot{u}_i^w - v u_{i,R}^w\right)d\Omega + nS_r \int_\Gamma \delta p^w n_i\left(\dot{u}_i^w - v u_{i,R}^w\right)d\Gamma + nS_r \int_\Omega \delta p^w_{,i}\left(\dot{u}_i^s - v u_{i,R}^s\right)d\Omega$$

$$- nS_r \int_\Gamma \delta p^w n_i\left(\dot{u}_i^s - v u_{i,R}^s\right)d\Gamma$$

The mass conservation equation for pore water can be expressed in a discrete format.

By multiplying both sides of equation (21), the mass conservation equation for pore gas, with the test function $\boldsymbol{\delta p^a}$, its equivalent integral weak form is derived. Integration by parts yields the following form.

$$n(1-S_r)\int_\Omega \delta p^a\left[\left(\dot{u}_{i,i}^a - v\nabla u_{i,R}^a\right) - \left(\dot{u}_{i,i}^s - v\nabla u_{i,R}^s\right)\right]d\Omega$$

$$= -n(1-S_r)\int_\Omega \delta p^a_{,i}\left(\dot{u}_i^a - v u_{i,R}^a\right)d\Omega + n(1-S_r)\int_\Gamma \delta p^a n_i\left(\dot{u}_i^a - v u_{i,R}^a\right)d\Gamma$$

$$+ n(1-S_r)\int_\Omega \delta p^a_{,i}\left(\dot{u}_i^s - v u_{i,R}^s\right)d\Omega - n(1-S_r)\int_\Gamma \delta p^a n_i\left(\dot{u}_i^s - v u_{i,R}^s\right)d\Gamma$$

The mass conservation equation for pore gas can be expressed in a discrete format.

Reference

[1] P.-E. Gautier, Slab track: Review of existing systems and optimization potentials including very high speed, Constr. Build. Mater., 92 (2015) 9-15.

[2] C. Esveld, Recent developments in high-speed track, In: 1st Int. Conf. on Road and Rail Infrastructure. Zagreb (Croatia): University of Zagreb, (2010).

[3] K. Inaba, H. Tanigawa, H. Naito, A study on evaluating supporting condition of railway track slab with impact acoustics and non-defective machine learning, Constr. Build. Mater., 373 (2023).

[4] L. Auersch, S. Said, Track-soil dynamics – Calculation and measurement of damaged and repaired slab tracks, Transp. Geotech., 12 (2017) 1-14.

[5] Z. Wan, W. Xu, Z. Zhang, C. Zhao, X. Bian, In-situ investigation on mud pumping in ballastless high-speed railway and development of remediation method, Transp. Geotech., 33 (2022).

[6] Y. Wu, H. Fu, X. Bian, Y. Chen, Impact of extreme climate and train traffic loads on the performance of high-speed railway geotechnical infrastructures, Journal of Zhejiang University-SCIENCE A, 24 (2023) 189-205.

[7] J. Huang, Q. Su, T. Liu, W. Wang, Behavior and Control of the Ballastless Track-Subgrade Vibration Induced by High-Speed Trains Moving on the Subgrade Bed with Mud Pumping, Shock Vib., 2019 (2019) 1-14.

[8] Z. Lin, F. Niu, X. Li, A. Li, M. Liu, J. Luo, Z. Shao, Characteristics and controlling factors of frost heave in high-speed railway subgrade, Northwest China, Cold Reg. Sci. Technol., 153 (2018) 33-44.

[9] X. Cui, H. Xiao, Interface Mechanical Properties and Damage Behavior of CRTS II Slab Track considering Differential Subgrade Settlement, KSCE J. Civ. Eng., 25 (2021) 2036-2045.

[10] X. Bian, Z. Wan, C. Zhao, Y. Cui, Y. Chen, Mud pumping in the roadbed of ballastless high-speed railway, Géotechnique, 73 (2023) 614-628.

[11] M.A. Biot, General theory of three‐dimensional consolidation, J. Appl. Phys., 12 (1941) 155-164.

[12] M.A. Biot, Theory of propagation of elastic waves in a fluid‐saturated porous solid. II. Higher frequency range, The Journal of the acoustical Society of america, 28 (1956) 179-191.

[13] A. Esmaeili Moghadam, R. Rafiee-Dehkharghani, Optimal design of wave barriers in dry and saturated poroelastic grounds using Covariance Matrix Adaptation Evolution Strategy, Comput. Geotech., 133 (2021).

[14] L.H. Tong, H. Ding, L. Zeng, D.X. Geng, C.J. Xu, On the dynamic response of a poroelastic medium subjected to a moving load based on nonlocal Biot theory, Comput. Geotech., 134 (2021).

[15] O. Zienkiewicz, T. Shiomi, Dynamic behaviour of saturated porous media; the generalized Biot formulation and its numerical solution, Int. J. Numer. Anal. Methods Geomech., 8 (1984) 71-96.

[16] B. Simon, O. Zienkiewicz, D. Paul, An analytical solution for the transient response of saturated porous elastic solids, Int. J. Numer. Anal. Methods Geomech., 8 (1984) 381-398.

[17] B. Simon, J.S. Wu, O. Zienkiewicz, D. Paul, Evaluation of u‐w and u‐π finite element methods for the dynamic response of saturated porous media using one‐dimensional models, Int. J. Numer. Anal. Methods Geomech., 10 (1986) 461-482.

[18] O. Zienkiewicz, C. Chang, P. Bettess, Drained, undrained, consolidating and dynamic behaviour assumptions in soils, Geotechnique, 30 (1980) 385-395.

[19] G. Gao, J. Zhang, J. Chen, J. Bi, Investigation of saturation effects on vibrations of nearly saturated ground due to moving train loads using 2.5 D FEM, Soil Dyn. Earthquake Eng., 158 (2022) 107288.

[20] G.Y. Gao, Q.S. Chen, J.F. He, F. Liu, Investigation of ground vibration due to trains moving on saturated multi-layered ground by 2.5D finite element method, Soil Dyn. Earthquake Eng., 40 (2012) 87-98.

[21] X. Bian, J. Hu, D. Thompson, W. Powrie, Pore pressure generation in a poro-elastic soil under moving train loads, Soil Dyn. Earthquake Eng., 125 (2019).

[22] H.Y. Zhao, B. Indraratna, T. Ngo, Numerical simulation of the effect of moving loads on saturated subgrade soil, Comput. Geotech., 131 (2021).

[23] Z. Lu, R. Fang, H. Yao, C. Dong, S. Xian, Dynamic responses of unsaturated half-space soil to a moving harmonic rectangular load, Int. J. Numer. Anal. Methods Geomech., 42 (2018) 1057-1077.
[24] C. Tang, Z. Lu, H. Yao, S. Guo, X. Huang, J. Liu, Semianalytical Solution for Dynamic Responses of Railway Track System on Unsaturated Poroelastic Half-Space Subjected to Moving Trainload, Int. J. Geomech., 21 (2021).
[25] R. Fang, Z. Lu, H. Yao, X. Luo, M. Yang, Study on dynamic responses of unsaturated railway subgrade subjected to moving train load, Soil Dyn. Earthquake Eng., 115 (2018) 319-323.
[26] X. Li, O. Zienkiewicz, Y. Xie, A numerical model for immiscible two-phase fluid flow in a porous medium and its time domain solution, Int. J. Numer. Methods Eng., 30 (1990) 1195-1212.
[27] S.-J. Feng, Y.-C. Li, J.-P. Li, Prediction and mitigation analysis of railway-induced vibrations of a layered transversely isotropic ground comprising different media with a hybrid 2.5-D method, Comput. Geotech., 159 (2023).
[28] Y.B. Yang, H.H. Hung, A 2.5 D finite/infinite element approach for modelling visco-elastic bodies subjected to moving loads, Int. J. Numer. Methods Eng., 51 (2001) 1317-1336.
[29] G. Gao, S. Yao, J. Yang, J. Chen, Investigating ground vibration induced by moving train loads on unsaturated ground using 2.5 D FEM, Soil Dyn. Earthquake Eng., 124 (2019) 72-85.
[30] K.K. Ang, J. Dai, Response analysis of high-speed rail system accounting for abrupt change of foundation stiffness, J. Sound Vib., 332 (2013) 2954-2970.
[31] C. Koh, J. Ong, D. Chua, J. Feng, Moving element method for train-track dynamics, Int. J. Numer. Methods Eng., 56 (2003) 1549-1567.
[32] M.T. Tran, K.K. Ang, V.H. Luong, Vertical dynamic response of non-uniform motion of high-speed rails, J. Sound Vib., 333 (2014) 5427-5442.
[33] V.H. Luong, T.N.T. Cao, J. Reddy, K.K. Ang, M.T. Tran, J. Dai, Static and dynamic analyses of Mindlin plates resting on viscoelastic foundation by using moving element method, Int. J. Struct. Stab. Dyn., 18 (2018) 1850131.
[34] M. Chen, Y. Sun, W. Zhai, High efficient dynamic analysis of vehicle–track–subgrade vertical interaction based on Green function method, Veh. Syst. Dyn., 58 (2019) 1076-1100.
[35] X. Lei, High speed railway track dynamics, Springer2017.
[36] K. Liu, Q. Su, F. Yue, B. Liu, R. Qiu, T. Liu, Effects of suffosion-induced contact variation on dynamic responses of saturated roadbed considering hydro-mechanical coupling under high-speed train loading, Comput. Geotech., 113 (2019) 103095.
[37] A.W. Bishop, G. Blight, Some aspects of effective stress in saturated and partly saturated soils, Geotechnique, 13 (1963) 177-197.
[38] K. Tuncay, M. Corapcioglu, Wave propagation in poroelastic media saturated by two fluids, (1997).
[39] M. Xu, Investigation on Dynamic Response of Unsaturated Soils and Foundation, China: South China University of Technology (2010).
[40] G. Wanner, E. Hairer, Solving ordinary differential equations II, Springer Berlin Heidelberg New York1996.
[41] J. Cash, Second derivative extended backward differentiation formulas for the numerical integration of stiff systems, SIAM J. Numer. Anal., 18 (1981) 21-36.
[42] W. Li, C. Wei, Stabilized low-order finite elements for strongly coupled poromechanical problems, Int. J. Numer. Methods Eng., 115 (2018) 531-548.
[43] T. Li, Q. Su, K. Shao, J. Liu, Numerical Analysis of Vibration Responses in High-Speed Railways considering Mud Pumping Defect, Shock Vib., 2019 (2019) 1-11.
[44] Z. Ye, Z.Y. Ai, Y. Chen, L. Chen, Vibration analysis of a beam on a layered transversely isotropic unsaturated subgrade subjected to a moving load, Appl. Math. Modell., 121 (2023) 204-216.
[45] J. Zhang, Z. Lu, C. Tang, J. Liu, H. Yao, Forward calculation of displacement fields with multilayered unsaturated highway system induced by falling weight deflectometer using dynamic response method, Transp. Geotech., 38 (2023).
[46] D. Theodorakopoulos, A. Chassiakos, D. Beskos, Dynamic effects of moving load on a poroelastic soil medium by an approximate method, Int. J. Solids Struct., 41 (2004) 1801-1822.
[47] T. Xin, P. Wang, Y. Ding, Effect of Long-Wavelength Track Irregularities on Vehicle Dynamic Responses, Shock Vib., 2019

(2019) 1-11.

[48] D. Connolly, P.A. Costa, Geodynamics of very high speed transport systems, Soil Dyn. Earthquake Eng., 130 (2020) 105982.

[49] D.P. Connolly, K. Dong, P. Alves Costa, P. Soares, P.K. Woodward, High speed railway ground dynamics: a multi-model analysis, Int. J. Rail Transp., 8 (2020) 324-346.

[50] H. Jiang, Y. Li, Y. Wang, K. Yao, Z. Yao, Z. Xue, X. Geng, Dynamic performance evaluation of ballastless track in high-speed railways under subgrade differential settlement, Transp. Geotech., 33 (2022) 100721.